metals

Article

Corrosion Behaviour of Heat-Treated Cold Spray Nickel Chromium/Chromium Carbides

Cedric Tan , Kannoorpatti Krishnan * and Naveen Kumar Elumalai

Advanced Manufacturing Alliance, Energy and Resources Institute, Faculty of Science and Technology and Environment, Charles Darwin University, Darwin, NT 0909, Australia; cedric.tan@cdu.edu.au (C.T.); naveenkumar.elumalai@cdu.edu.au (N.K.E.)
* Correspondence: krishnan.kannoorpatti@cdu.edu.au

Abstract: Chromium carbide powder agglomerated with nickel/chrome was deposited using a cold spray process onto a mild steel substrate. The deposits were heat-treated at 650 °C and 950 °C in ambient conditions to reduce porosity and improve adhesion between powder particles. The corrosion behaviour of these cold-sprayed materials was studied in artificial seawater conditions using electrochemical techniques. Heat treatment at 650 °C was found to best improve corrosion resistance, while the 950 °C treatment performed better than the as-sprayed condition but lower than the 650 °C sample. Microstructural analysis revealed complex phase transformations and structural refinements with increasing heat treatment temperature. The crystallite size of both Cr_3C_2 and NiCr phases decreased, while microstrain and dislocation density increased due to heat treatment. The formation of and subsequent reduction in $Cr_{23}C_6$ content indicated a complex sequence of carbide dissolution, transformation, and precipitation processes. The 650 °C heat-treated sample demonstrated superior corrosion resistance, evidenced by the highest corrosion potential, lowest passive current, and largest charge transfer resistance. This enhanced performance was attributed to the formation of a more stable and protective passive film, optimal carbide dissolution, and a homogeneous microstructure. Meanwhile, the 950 °C treatment led to excessive carbide dissolution and formed increased interfaces between the carbide and matrix. Mechanical property changes were also observed, with carbide hardness significantly decreasing after corrosion testing. These findings highlight the critical role of controlled heat treatment in optimising the performance of cold-sprayed Cr_3C_2-NiCr coatings, demonstrating that achieving superior corrosion resistance requires a delicate balance between microstructural refinement, phase transformations, and preservation of coating integrity.

Keywords: hardfacing; corrosion; carbides; heat treatment; chromium; cold spray

check for updates

Citation: Tan, C.; Krishnan, K.; Elumalai, N.K. Corrosion Behaviour of Heat-Treated Cold Spray Nickel Chromium/Chromium Carbides. *Metals* **2024**, *14*, 1153. https://doi.org/10.3390/met14101153

Academic Editor: Changdong Gu

Received: 12 September 2024
Revised: 4 October 2024
Accepted: 8 October 2024
Published: 10 October 2024

1. Introduction

Cold spray deposition has emerged as a promising solid-state coating technology in recent years, offering unique advantages over traditional thermal spray methods [1,2]. This process involves accelerating powder particles to supersonic velocities and relies on plastic deformation upon impact for coating formation, allowing for the deposition of a wide range of materials without the thermal degradation associated with high-temperature processes [3,4]. Among the materials of interest for cold spray deposition are nickel chromium/chromium carbide (NiCr-CrC) cermets, which are widely used in applications requiring excellent wear and corrosion resistance at elevated temperatures, such as in aerospace, automotive, and power generation industries [5]. Furthermore, they have been used on structural repair to mitigate corrosion damage on substrates such as steel [6]. When used in wear resistance applications, the substrate is usually carbon steel. A review on the applications of cold spray was carried out by Singh et al. [7]. These cermet coatings combine the toughness of the metallic NiCr matrix with the hardness and wear resistance of chromium carbide particles, making them ideal for protecting components in harsh environments [8,9].

Traditionally, NiCr-CrC coatings have been applied through methods such as weld deposition, casting blocks, and thermal spraying [10]. Weld deposition and casting blocks, commonly used in the mining industry, are limited by equilibrium reactions that dictate the number of hard constituents (e.g., carbides) and offer minimal control over the size and distribution of carbides within the matrix, requiring post-welding treatment for further microstructural control [11]. Furthermore, while traditional deposition methods can produce thick, wear-resistant layers, they are often restricted to simple geometries and can induce significant heat-affected zones in the substrate material [12].

Thermal spraying, particularly high-velocity oxygen fuel (HVOF) spraying, has become the predominant method for applying NiCr-CrC coatings due to its versatility and ability to produce high-quality coatings [10]. However, HVOF and other thermal spray techniques have some inherent limitations when processing NiCr-CrC materials. The high temperatures involved in these processes can cause significant issues, including carbide dissociation, chromium oxidation, and element segregation [3,4]. Specifically, Cr_3C_2 may decompose to form Cr_7C_3 and $Cr_{23}C_6$, altering the intended microstructure and properties of the coating [13]. These thermal effects can reduce the available chromium for corrosion resistance and carbide formation, potentially compromising the coating's performance [14]. Furthermore, thermal sprayed coatings often contain oxides, porosities, and decomposed carbides, which can reduce wear and corrosion resistance [2].

To address these limitations, cold spray deposition has emerged as a promising alternative for applying NiCr-CrC coatings. Cold spray technology offers several advantages over traditional thermal spray methods for depositing NiCr-CrC coatings. The solid-state bonding and mechanical interlocking mechanism of cold spray eliminates powder melting, resulting in preservation of the original powder characteristics [1]. This makes cold spray particularly suitable for temperature-sensitive materials and tends to produce harder deposits due to work hardening [3,4]. Additionally, the process induces high compressive stresses in the deposits, which can be beneficial for fatigue resistance [2].

However, cold spray is not without its challenges, particularly when it comes to ceramic-rich materials like NiCr-CrC. The process requires ductile powders for effective deformation and bonding, which can be challenging for cermet materials [15]. Cold-sprayed coatings have issues with porosity and incomplete bonding between powder particles [16]. Furthermore, the high degree of plastic deformation during deposition can result in poor ductility in the final coating [16].

To address these limitations, post-deposition heat treatment is often employed to reduce porosity and improve ductility in cold-sprayed deposits [16]. Typically, this involves sintering at temperatures close to the melting point of the material. However, recent studies have shown that significant improvements in coating properties can be achieved even at lower temperatures, such as 450 °C for chromium carbide coatings [17]. Heat treatment of NiCr-CrC coatings can induce various transformations in the chromium carbides, depending on the temperature and atmosphere [16]. Oxidation of chromium in chromium carbides can occur, leading to the formation of a protective Cr_2O_3 layer [18]. However, at high temperatures and in the presence of oxygen, this oxide layer may change to a finely divided form, potentially affecting its protective properties [18].

The corrosion behaviour of NiCr-CrC coatings is of particular interest, especially considering potential microstructural changes induced by heat treatment. Sensitisation, a phenomenon observed in stainless steels at around 650 °C, could potentially occur in the NiCr matrix, affecting corrosion resistance [19]. Sensitisation has been reported in welded stainless steels where the regions adjacent to the grain boundaries are depleted of chromium, resulting in corrosion. Additionally, the dissolution and reformation of carbides, as observed in welded stabilised stainless steel, may influence the coating's overall performance [20].

Despite the growing interest in cold-sprayed NiCr-CrC coatings, research on their corrosion behaviour, particularly at room temperature, remains limited. Most studies have focused on high-temperature performance or wear resistance [21,22]. Thin chromium coatings (1 µm) have been applied on valve seatings, and it was found that the oxidation resistance at 900 °C was better than that of uncoated material [23,24]. Additionally, due to relatively recency of cold spray material, the majority of corrosion studies on NiCr-CrC coatings have been conducted on HVOF-sprayed samples rather than cold-sprayed ones [2]. This gap in knowledge is significant, as understanding the room temperature corrosion behaviour is crucial for applications where components may be exposed to corrosive environments during idle periods or maintenance.

The aim of this study is to address this research gap by investigating the room temperature corrosion properties of cold-sprayed NiCr-CrC coatings on mild steel substrates and exploring ways to improve their corrosion resistance in artificial seawater which would simulate conditions for a digger or dredger in seawater. Specifically, we assess the effects of post-deposition heat treatments at 650 °C and 950 °C on the coatings' microstructure, porosity, and corrosion resistance. Furthermore, we conduct an in-depth analysis of electrochemical processes at different interfaces within the coating structure to enhance our fundamental understanding of corrosion mechanisms in complex, multi-phase materials. By elucidating the complex interplay between processing conditions, microstructure, and corrosion resistance, this study provides a more comprehensive understanding of cermet coating behaviour and the factors affecting the corrosion resistance of cold-sprayed NiCr-CrC coatings. This research has significant implications for materials science and engineering, particularly in developing advanced corrosion-resistant coatings.

2. Experimental Procedure

2.1. Material Preparation

For this study, the commercially available powder WIP-C2 from Solvus Global was deposited using cold spray onto a mild steel plate from an as-received condition. The technical data sheet describes the powder as chrome carbide agglomerated with nickel/chrome in the composition of Cr-26Ni-3C and designed for hardness and impact resistance [25,26]. Other researchers for similar powders have found the main form of chromium carbides to be Cr_3C_2 [26]. From its data sheet, the expected particle size distribution is provided in Table 1 [25]:

Table 1. Particle size distribution.

D10% (µm)	D50% (µm)	D90% (µm)
19 ± 10%	27 ± 10%	45 ± 10%

This powder was sprayed using a WarpSPEE3D machine (SPEE3D Melbourne, VIC, Australia) [27] with deposition parameters as shown in Table 2: the machine uses a stationary nozzle through which the powder is accelerated to supersonic velocities and a robot arm with the substrate.

Table 2. Cold spray deposition parameters.

Parameter	Value
Gas	Compressed air
Temperature	800 °C
Pressure	30 bar
Working distance	20 mm
Coating thickness	4 mm
Layer thickness	1.8 mm (mild steel)

Heat treatment was undertaken in air to produce sintering and ensure bonding between particles. This alloy was heated from room temperature and left to cool in air after holding at different temperatures for 6 h. Table 3 describes the different temperatures used for heat treating the samples.

Table 3. Heat treatment parameters.

Name	Heat Treatment Temperature	Time (Hours)
Sample A	(No heat treatment)	N/A
Sample B	650 °C	6
Sample C	950 °C	6

Heat treatment at 650 °C was chosen to minimise oxidation of Cr_3C_2 whilst 950 °C was chosen as the upper limit for heat treatment [21,28].

Following the heat treatment, samples were cut to leave a flat 1 cm × 1 cm surface for microstructural observation and testing. These samples were electrically connected and fixed in epoxy, leaving only the flat surface exposed to serve as a working electrode. Samples were also polished to a 1 µm finish and etched with 5% Nital for microstructural observation.

For the environmental medium, artificial seawater was prepared in which the samples were exposed. This artificial seawater was created as per ASTM D1141-98, with the composition shown in Table 4 [29].

Table 4. Artificial seawater composition.

Compound	Concentration (g/L)
NaCl	24.53
$MgCl_2$	5.20
Na_2SO_4	4.09
$CaCl_2$	1.16
KCl	0.695
$NaHCO_3$	0.201
KBr	0.101
H_3BO_3	0.027
$SrCl_2$	0.025
NaF	0.03

2.2. Hardness Testing

The hardness of samples was evaluated both before and after corrosion testing. This was conducted using a DuraScan 70 machine, (Struers, Milton, QLD, Australia). A 0.1 kg load was used to separately measure the hardness of both carbides and the matrix and to view the indentations. Three separate tests at different locations were undertaken, with the average of the three results being reported in this investigation.

2.3. Electrochemical Testing

Electrochemical corrosion measurements were taken on each sample under a three-electrode cell setup and a Gamry 1010E potentiostat. With the samples serving as the working electrodes, Ag/AgCl- and platinum-coated electrodes served as the working and counter electrode, respectively. Before measurement, samples were polished as described in Section 2.1.

Before testing, samples were left exposed to the artificial seawater solution to allow the system to normalise for an hour. Open circuit potential (OCP) was then taken after 5 min, with potentiodynamic polarisation tests taken at a scan rate of 0.167 mV/s. This potentiodynamic polarisation was started from −0.2 V below OCP. Based on the potentiodynamic plots, potentiostatic points were chosen at different potentials to observe corrosion effects on the microstructures. Selection and analysis of this behaviour were undertaken using Gamry Echem Analyst software (version 7.9.0).

Similarly, electrochemical impedance spectroscopy (EIS) measurements for each sample were taken after exposing the samples to the artificial seawater solution for an hour. OCP was also recorded for 5 min before starting EIS tests. EIS was taken over the range from 0.1 to 100,000 Hz with ±10 mV.

2.4. Microscopy and Chemical Analysis

Deposited samples were studied by optical methods and Scanning Electron Microscopy. For optical characterisation, samples were observed using a Nikon Eclipse (Otwara, Japan, supplied by Struers Australia) MA100 microscope at a 50× objective. Microscopy images were analysed using imageJ software (version 1.54) for carbide volume fraction.

A Scanning Electron Microscope (PhenomXL) was also used to observe the microstructure and take Energy Dispersive X-ray Spectroscopy measurements both before and after corrosion. X-ray diffraction (XRD) measurements were carried out using Malvern PANanalytical Empyrean (Malvern Pananalytical, Sydney, NSW, Australia) to study the phases and phase changes both before and after heat treatment. XRD equipment was run using a copper target, and the parameters used were 2θ = 20–90°, step size = 0.0394°, and a time of 300 s per step.

3. Results

3.1. Microstructural Characterisation

The top side of the deposits was characterised using optical microscopy and SEM, as seen in Figures 1–3. The figures show ovular primary carbides are surrounded by a eutectic matrix structure. Dark voids are present in the non-heat-treated Sample A and the 650HT Sample B. Fewer of these voids appear after heat treatment after 950 °C, as can be more easily seen in the optical microscopy pictures in Figures 1–3. The formation of such voids is noted in the literature to be more likely due to carbide particle pullout rather than "true" pores within the coating [6].

The samples heat-treated at 950 °C show a marked carbide decomposition compared to the samples heat-treated at 650 °C.

The number and size of carbides were evaluated from the optical microscopy pictures. This was carried out using three equally sized images from each sample, with typical surfaces as shown previously in Figures 1–3.

From Table 5, it can be seen that heat treatment decreased both the average size and number of carbides. This trend appears consistent as heat treatment temperature increases. For instance, the mean carbide size decreases from 154 μm^2 to 138 μm^2 to 98.7 μm^2 as heat treatment temperature increases from 650 °C to 950 °C. Similarly, the maximum carbide size found on the 950HT Sample C was almost half that of the maximum carbide found in the non-heat-treated original sample (322 μm^2 and 628 μm^2, respectively). Given this reduction in size and number of the carbides, this optical analysis indicates that the chromium carbides increasingly dissolve into the matrix as heat treatment temperature also increases.

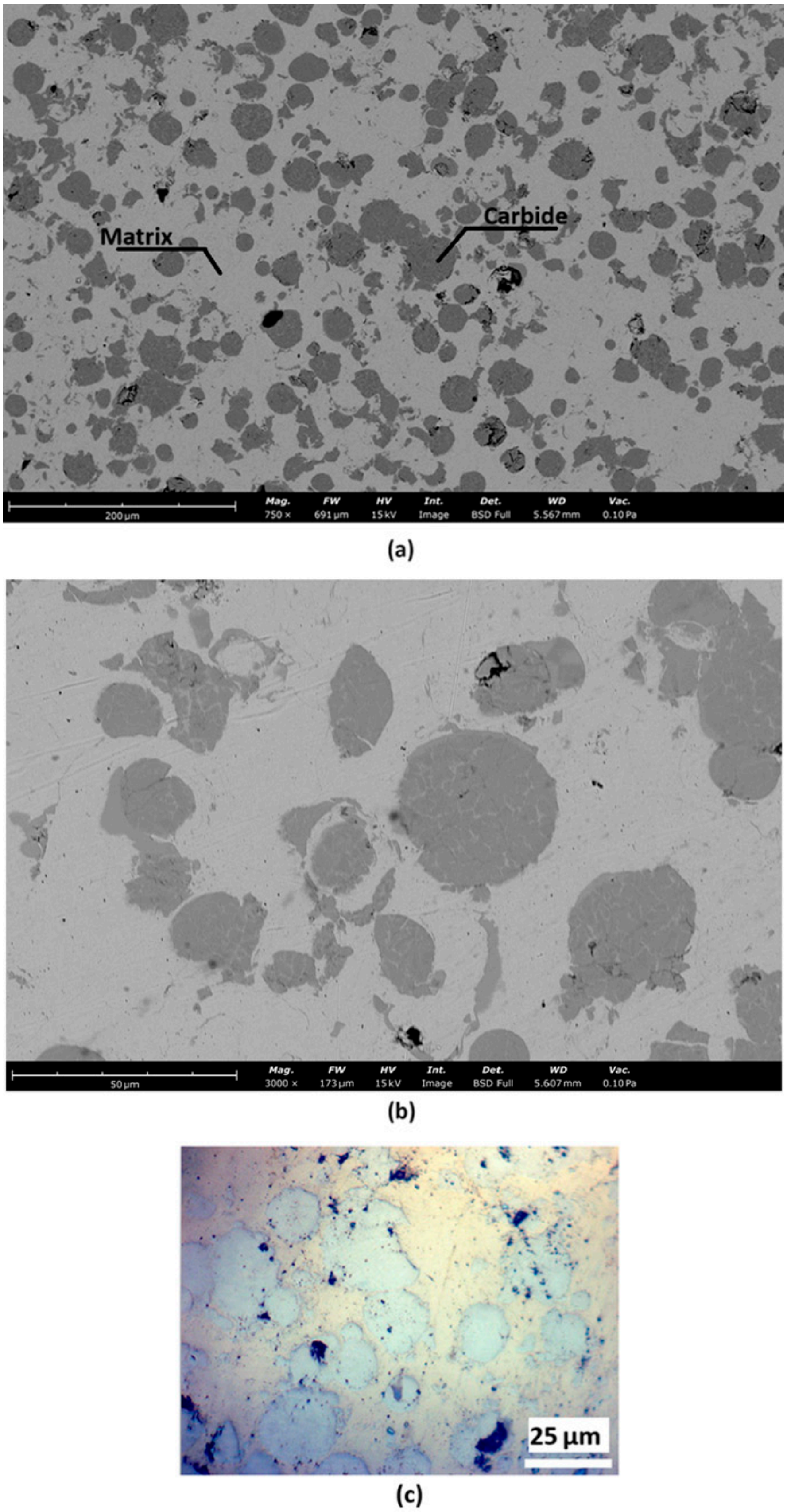

(a)

(b)

(c)

Figure 1. Microstructure of Sample A (non-heat-treated) showing primary carbides surrounded by NiCr matrix as well as voids for (**a**) SEM at lower magnification, (**b**) SEM at higher magnification, and (**c**) optical microscopy.

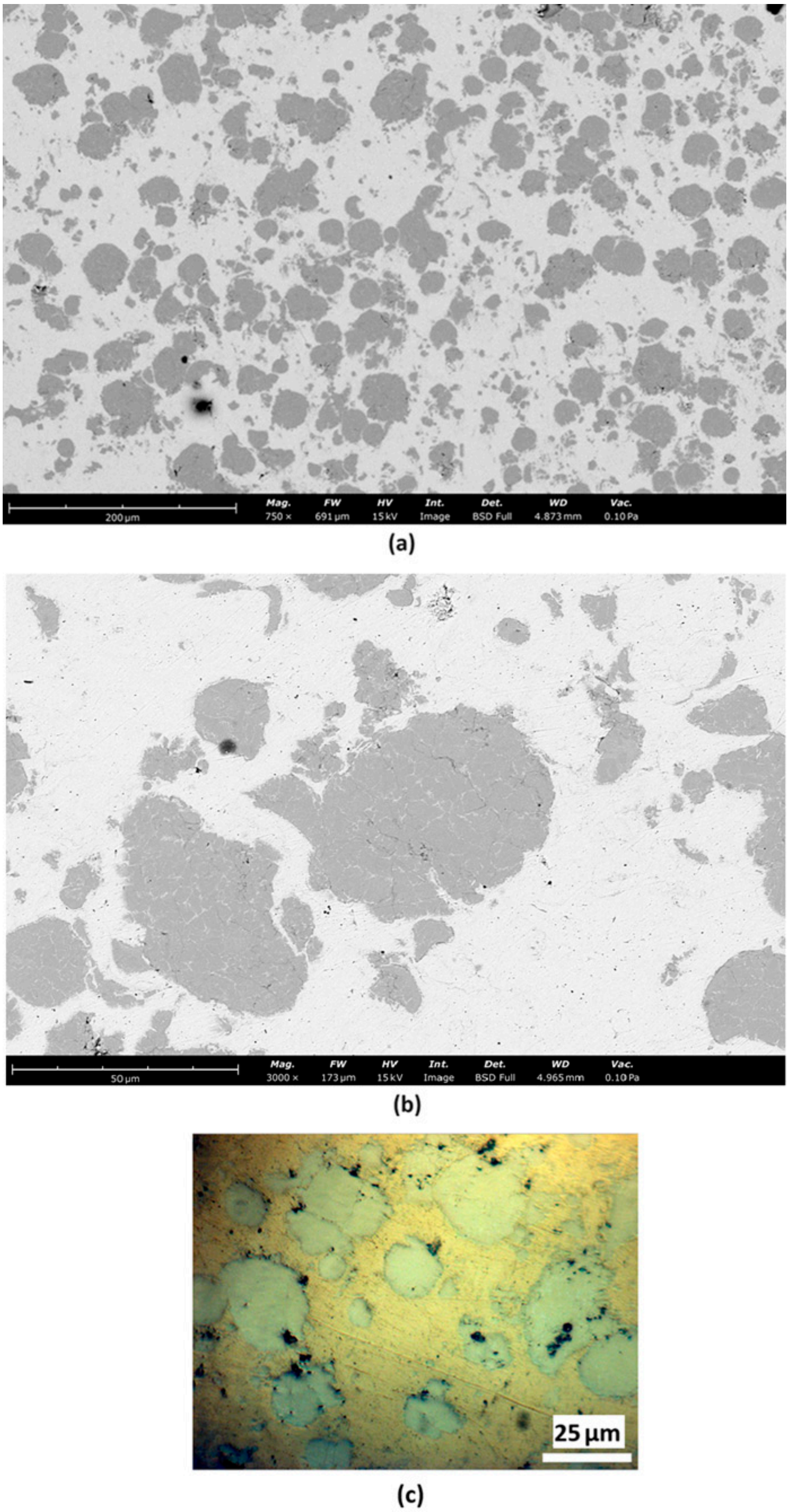

Figure 2. Microstructure of Sample B heat-treated at 650 °C for (**a**) SEM at lower magnification, (**b**) SEM at higher magnification, and (**c**) optical microscopy.

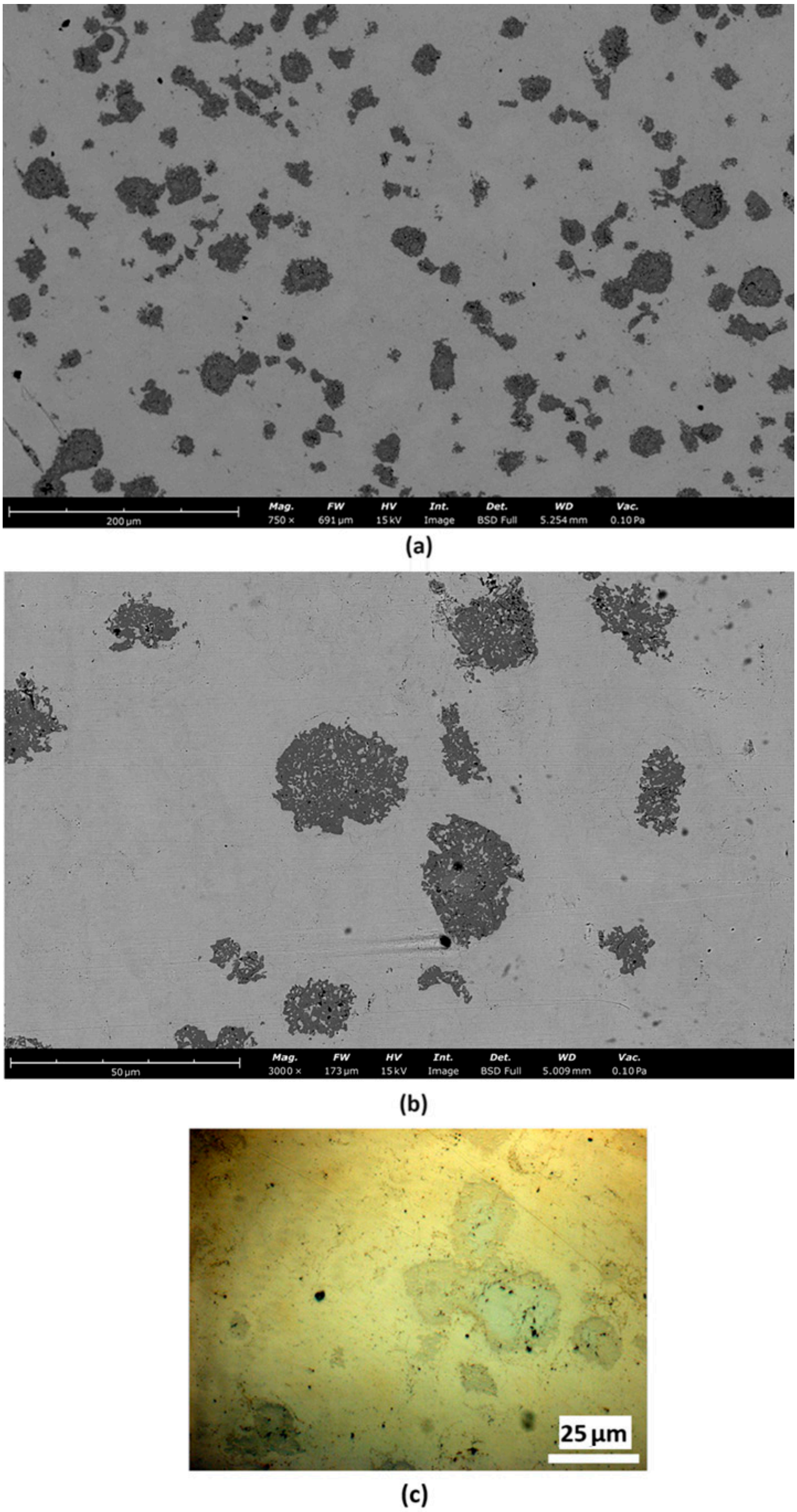

Figure 3. Microstructure of Sample C heat-treated at 950 °C for (**a**) SEM at lower magnification, (**b**) SEM at higher magnification, and (**c**) optical microscopy.

Table 5. Carbide distribution from Figures 1–3.

Sample	Mean Carbide Size (µm^2)	Min Carbide Size (µm^2)	Max Carbide Size (µm^2)	SD (µm^2)	Total No. of Carbides
noHT Sample A	154	9	628	6.1	145
650HT Sample B	138	8	504.6	7.4	122
950HT Sample C	98.7	5.5	322	5.5	90

Similar quantification of surface voids was undertaken using images such as those within Figures 1–3. As with quantification of carbides in imageJ, this was performed using three equally sized images from each sample. The results for these measurements are shown in Table 6.

Table 6. Void estimation via imageJ from Figures 1–3.

Sample	Mean Void Size (µm^2)	Min Void Size (µm^2)	Max Void Size (µm^2)	SD (µm^2)	Total No. of Voids
noHT Sample A	9	0.4	189	0.5	121
650HT Sample B	8	0.3	170	0.2	75
950HT Sample C	4	0.3	46	0.1	35

Quantification in this manner confirms the reduction in both average size and number of voids with increasing heat treatment. Interestingly, the average void size for the 650HT Sample B appears to remain close to that for the noHT Sample A (8 µm^2 compared to 9 µm^2), as does the maximum void size (170 vs. 189 µm^2), despite having a significantly lower number of voids (75 compared to 121). This suggests that at this heat treatment temperature, the smaller voids were the most reduced, whilst the larger voids only began to shrink slightly.

SEM-EDS analysis of the uncorroded samples was also undertaken. As with the optical microscopy, the SEM imagery showed ovular-shaped chromium carbides surrounded by a matrix material. Elemental analysis by EDS was conducted on the matrix and carbides. Representative locations for the carbide and matrix EDS analysis are shown in Figure 4.

From this, the comparison of elemental compositions of the carbides and the matrix between all samples in their as-sprayed state and post-heat treatments is shown in Tables 7 and 8.

Table 7. Matrix comparison of sample compositions via EDS (wt%).

Label	C	Cr	Ni	Total
Sample A (noHT)	2.8	7.9	89.3	100
Sample B (HT 650 °C)	1.90	10.5	87.6	100
Sample C (HT 950 °C)	1.8	20.6	77.6	100

Table 8. Carbide comparison of sample compositions via EDS (wt%).

Label	C	Cr	Ni	Si	Total
Sample A (noHT)	2.3	86.6	10.5	0.6	100
Sample B (HT 650 °C)	2.90	85.4	11.7	-	100
Sample C (HT 950 °C)	3.41	81.6	14.9	-	100

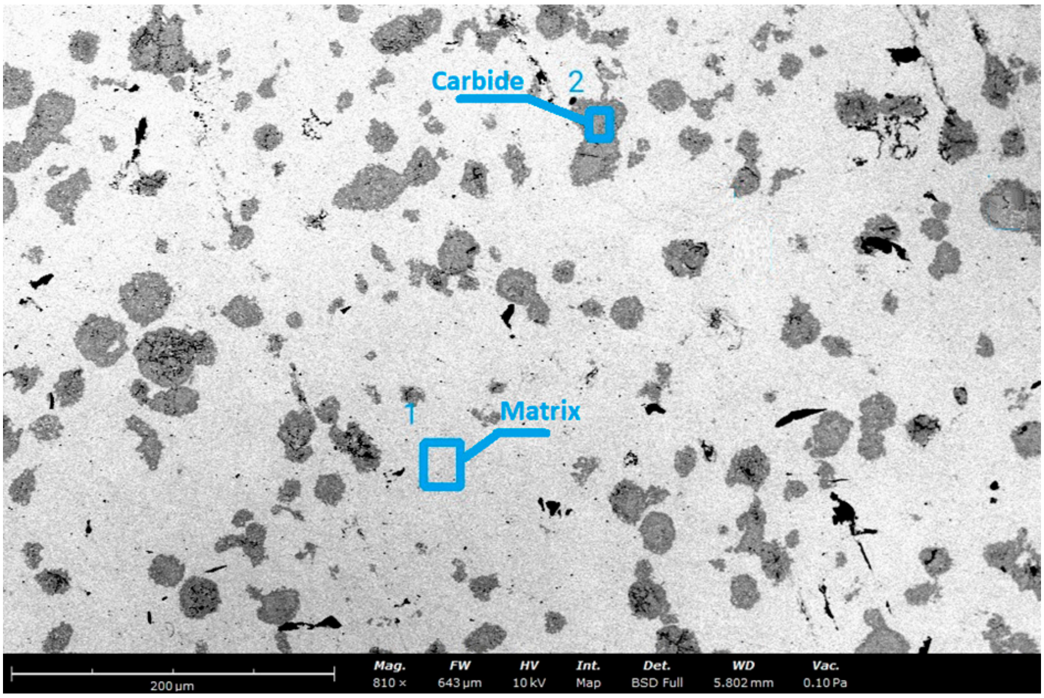

Figure 4. SEM-EDS surface indicating locations of matrix and carbide analysis, with example at 950 °C.

From Table 7, the noHT Sample A had the highest nickel content in the matrix, at 89.3 wt%. This nickel content in the matrix decreases with increasing heat treatment temperature, from 87.6 to 77.6 wt% at 650 °C and 950 °C, respectively. Similarly, in the as-sprayed state, chromium was found to be 7.9 wt% in the matrix for the original noHT Sample A. This increased to 10.5%Cr in the 650HT Sample B and 20.6%Cr for the 950HT Sample C.

The composition of the carbides is provided in Table 8. The composition of the carbides for the noHT Sample A showed the highest chromium content at 86.6 wt% and the lowest nickel content at 10.5%. With increasing heat treatment temperatures, there is a decrease in the wt% of chromium (85.4% to 81.6%) and an increase in the wt% of nickel (11.7% to 14.9%), respectively. This shows that it is likely that these carbides dissolve during heat treatment. This dissolution increases as heat treatment temperature increases. At 950HT, nickel content increased to 14.9% from 10.5 wt% in the noHT Sample A. This increase in nickel is most likely from the matrix. This is further supported by the optical microscopy results in Table 5 showing a decrease in the size and number of carbides during heat treatment.

X-ray diffraction (XRD) was also used to gauge changes in microstructural composition during heat treatment. This confirmed the presence of Cr_3C_2 peaks at $2\theta \approx 53°$ and 77° [26,30] as well as Ni/NiCr at $2\theta \approx 44°$ [26], as seen in Figure 5. Closer analysis of the XRD spectrum over 35–55° also reveals chromium carbides present in the form $Cr_{23}C_6$, as seen in Figure 6.

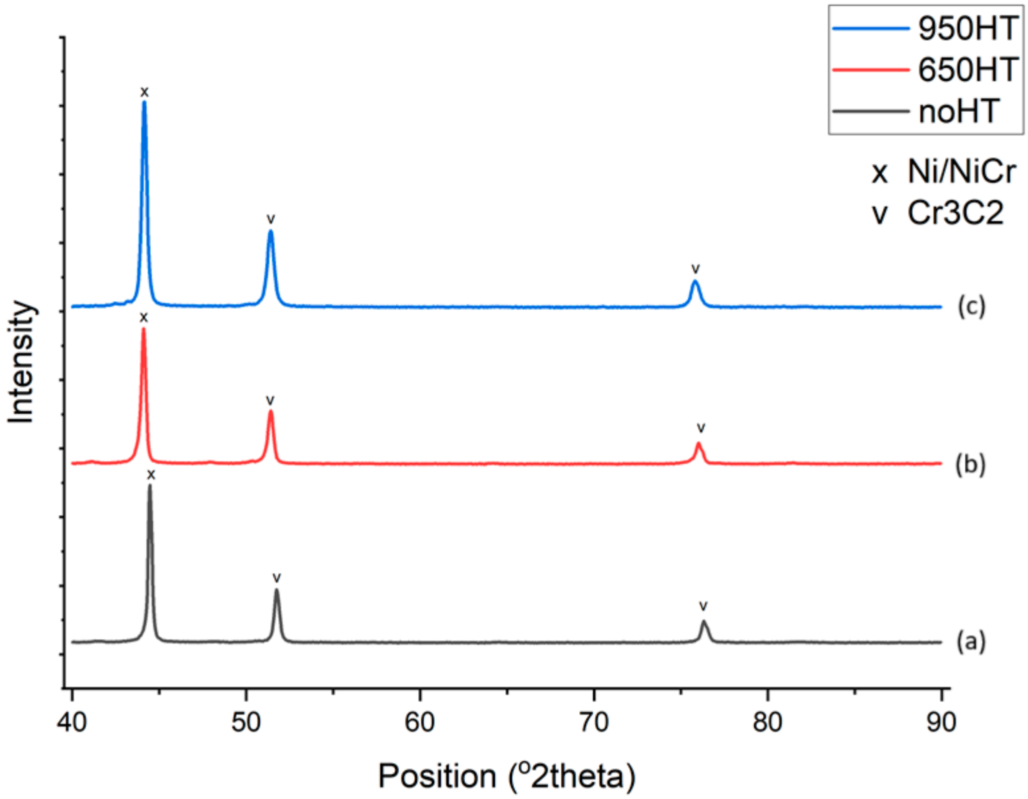

Figure 5. XRD for 2θ = 40–90°: (**a**) noHT Sample A, (**b**) 650HT Sample B, and (**c**) 950HT Sample C.

Rietveld analysis was conducted on the XRD spectra in order to gauge changes in the proportion of compounds using High Score software (version 5.2). The analysis was carried out in the range of 2θ = 35–55° where chromium carbide is expected. These results found that $Cr_{23}C_6$ content grew from 8.2% in the noHT Sample A to 13.9% in 650HT Sample B before reducing again to 6.4% in the 950HT Sample C, with nickel/nickel chromium being the remaining proportion to balance. This indicates that carbides were increasingly transformed with heat treatment into a more stable $Cr_{23}C_6$ state at 650 °C, whilst at 950 °C these carbides were being dissolved back into the matrix. It is important to note that although compositional percentage changes for $Cr_{23}C_6$ are given through this analysis, these are not the true compositional values due to the lack of Cr_3C_2 analysis.

XRD data can also be used to calculate other parameters such as crystallite size, microstrain, and dislocation density, as they provide insights into the crystallographic changes with the microstructural evolution due to heat treatment. Origin software (Version 10.1.5.132) was used to find the angle position (2θ) and full width at half maximum (β) of the peaks. Using a wavelength λ of 1.54 (for the copper target) and Equations (1)–(3), crystallite size, microstrain, and dislocation density were calculated [30]. The results are provided in Table 9 and in Figures 7–9.

$$Crystallite\ Size = \frac{0.94\lambda}{\beta cos\theta} \tag{1}$$

$$Microstrain = \frac{\beta}{4tan\theta} \tag{2}$$

$$Dislocation\ Density = (Crystallite\ Size)^{-1} \tag{3}$$

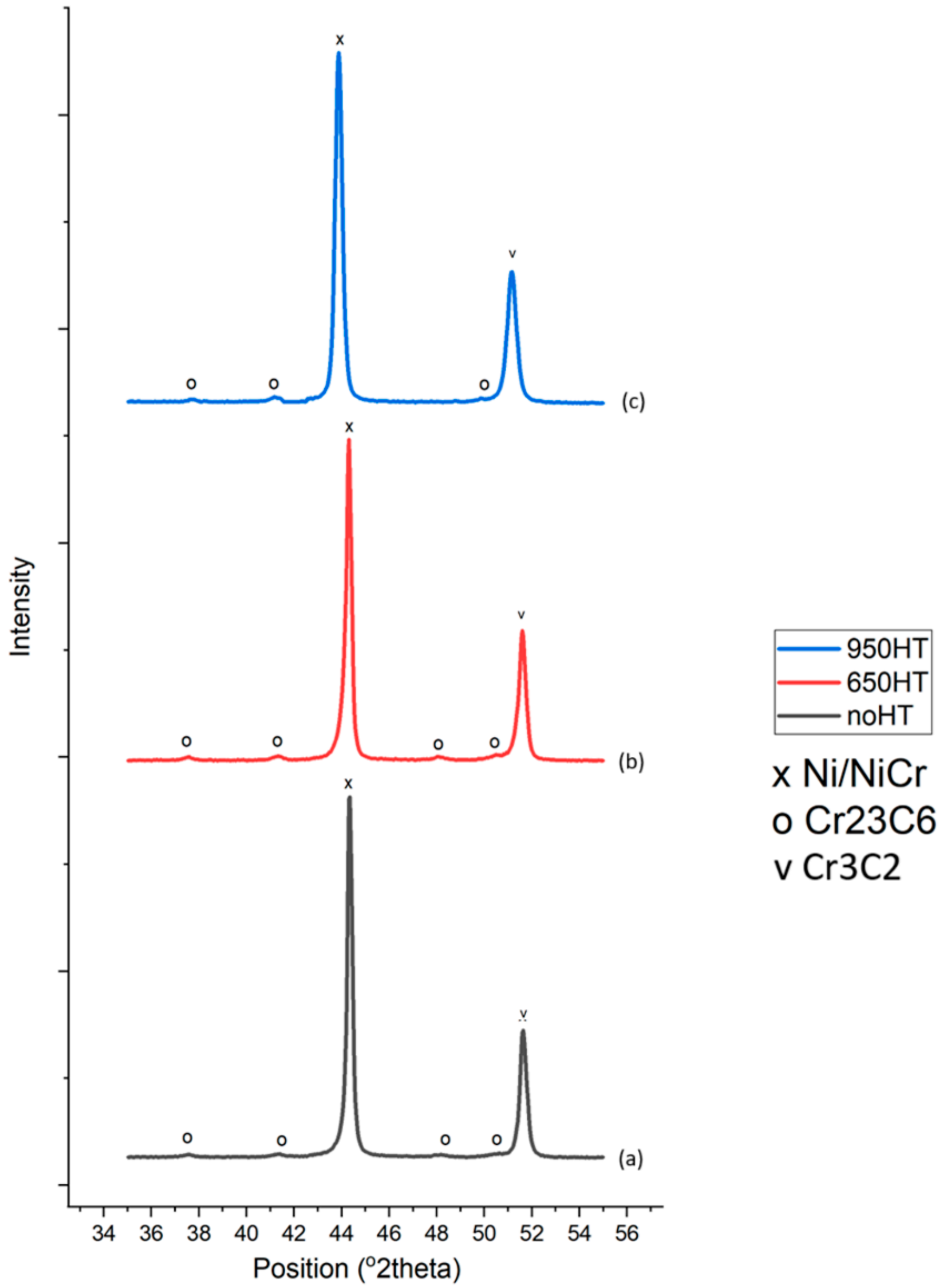

Figure 6. XRD for 2θ = 35–55°: (**a**) noHT Sample A, (**b**) 650HT Sample B, and (**c**) 950HT Sample C.

Table 9. Calculated XRD parameter values.

Peak Type	Alloy	2θ (°)	β (°)	D (nm)	Microstrain (ε)	Dislocation Density (10^{-9} m^{-2})
Cr_3C_2	noHT	64.1	0.420	23.3	0.00293	0.00184
Cr_3C_2	650HT	63.7	0.461	21.2	0.00323	0.00222
Cr_3C_2	950HT	63.6	0.532	18.3	0.00374	0.00297
NiCr	noHT	44.8	0.277	32.4	0.00295	0.000952
NiCr	650HT	44.1	0.344	26.1	0.0037	0.00147
NiCr	950HT	44.1	0.368	24.3	0.00396	0.00169

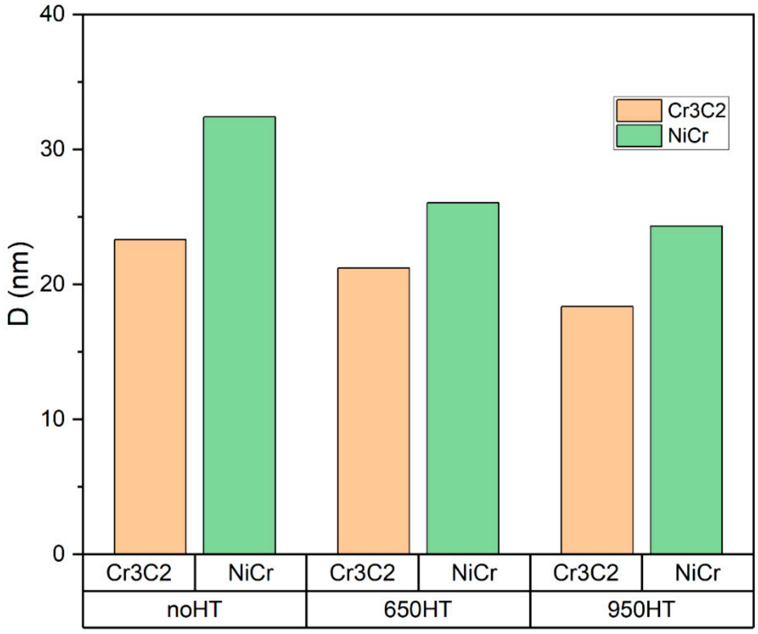

Figure 7. Crystallite sizes of Cr_3C_2 and NiCr.

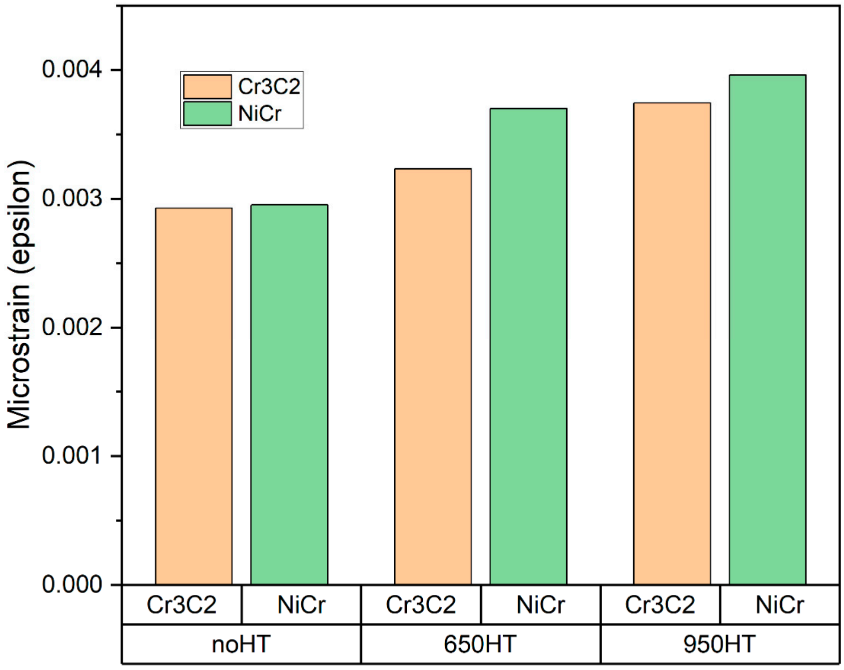

Figure 8. Microstrain values of Cr_3C_2 and NiCr.

The microstructural evolution of Cr_3C_2-NiCr coatings subjected to heat treatment at varying temperatures reveals complex phase transformations and structural refinements that significantly impact the coating's properties. In the as-sprayed state, the XRD pattern reveals two primary phases: Cr_3C_2 (chromium carbide) and the NiCr matrix. The Cr_3C_2 phase is identified by strong peaks at 2θ values of approximately 53° and 77°, confirming the presence of the intended hard carbide [31]. The face-centred cubic (FCC) nickel/chromium solid solution matrix is evidenced by peaks at 2θ values around 44° [26]. The broad, asymmetric nature of these peaks suggests some degree of alloying and potential nanocrystalline or amorphous structure in the as-sprayed matrix.

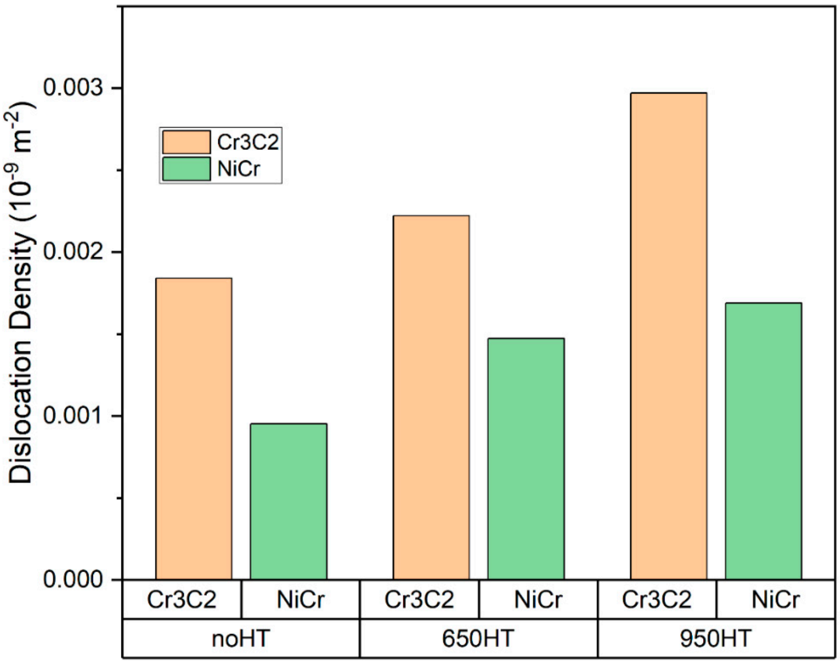

Figure 9. Dislocation densities of Cr_3C_2 and NiCr.

Heat treatment at 650 °C induces several notable changes in the coating's microstructure. The relative intensity of the Cr_3C_2 peaks increases compared to the as-sprayed condition, suggesting potential precipitation of additional carbides from the supersaturated matrix. A small shift to higher 2θ angles is observed for the NiCr matrix peaks, indicating a reduction in lattice parameters due to the precipitation of dissolved carbide-forming elements. Interestingly, small peaks corresponding to $Cr_{23}C_6$ are detected, with quantitative analysis revealing approximately 13.9% $Cr_{23}C_6$ content. This indicates the onset of carbide transformation at 650 °C, consistent with the known phase transformations in the Cr-C system at this temperature [19].

Further heat treatment at 950 °C leads to more pronounced microstructural changes. All peaks become more intense, indicating continued grain growth and stress relief. The relative intensity of the Cr_3C_2 peaks increases further, suggesting more extensive carbide precipitation and growth. Surprisingly, the $Cr_{23}C_6$ content decreases to 6.4% compared to the 650 °C sample, which may be due to either dissolution back into the matrix or transformation to other carbide phases not clearly resolved in the XRD pattern.

The XRD data also provide insights into the changes in crystallite size (D), microstrain (ε), and dislocation density for both the Cr_3C_2 and NiCr phases. For the Cr_3C_2 phase, the crystallite size decreases from 23.32 nm in the as-sprayed condition to 21.21 nm at 650 °C and further to 18.35 nm at 950 °C. Concurrently, the microstrain in the Cr_3C_2 phase increases from 0.00293 to 0.00323 at 650 °C and 0.00374 at 950 °C, indicating a rise in lattice distortions and defects. The dislocation density also shows an increasing trend, rising from 0.00184×10^{-9} m^{-2} to 0.00222×10^{-9} m^{-2} at 650 °C and 0.00297×10^{-9} m^{-2} at 950 °C.

The NiCr matrix also exhibits similar trends in its microstructural evolution. The crystallite size of the matrix phase decreases from 32.41 nm in the as-sprayed condition to 26.05 nm at 650 °C and 24.33 nm at 950 °C, indicating a refinement of the matrix crystal structure. The microstrain in the NiCr matrix increases from 0.00295 to 0.00370 at 650 °C and 0.00396 at 950 °C, suggesting a rise in lattice distortions. The dislocation density shows a significant increase from $(9.52 \times 10^{-4}) \times 10^{-9}$ m^{-2} to $(1.47 \times 10^{-3}) \times 10^{-9}$ m^{-2} at 650 °C and $(1.69 \times 10^{-3}) \times 10^{-9}$ m^{-2} at 950 °C.

These microstructural changes can be attributed to several mechanisms occurring during heat treatment. The partial transformation of Cr_3C_2 to $Cr_{23}C_6$ at higher temperatures introduces additional phase interfaces and stresses. The relaxation of residual stresses from the cold spray process is coupled with the generation of new thermal stresses during heat treatment. The refinement of the matrix structure occurs through the precipitation of dissolved elements and the formation of new interface boundaries. The observed microstructural evolution has important implications for the coating's performance. The refinement of both carbide and matrix structures could potentially lead to changes in hardness. However, the increases in microstrain and dislocation density may affect the coating's ability to accommodate deformation.

The XRD results correlate well with the microstructural characterisation data, which show a decrease in average carbide size from 154 μm^2 in the non-heat-treated condition to 98.7 μm^2 at 950 °C, consistent with the reduction in Cr_3C_2 peak intensities. The increase in matrix Cr content from 7.9 wt% to 20.6 wt% at 950 °C (shown in Table 7) aligns with the observed peak shifts in the NiCr matrix, confirming significant chromium diffusion. The decrease in carbide Cr content from 86.6 wt% to 81.6 wt% at 950 °C supports the XRD evidence of carbide dissolution and transformation.

The microstructural evolution during heat treatment exhibits some intriguing and atypical behaviours. The decrease in crystallite size, coupled with increases in dislocation density and microstrain, suggests a complex interplay of mechanisms occurring within the alloy system. One possibility is the precipitation of fine secondary phases, such as carbides, within the NiCr matrix during heat treatment. It could be speculated that these precipitates may act as barriers to grain growth and even promote the formation of new, smaller grains. Additionally, if the heat treatment temperature falls within a specific range, it might trigger recrystallisation processes, leading to the formation of new, finer phases from the highly deformed cold-sprayed structure [19].

The increase in dislocation density is equally unusual, as annealing typically reduces dislocation content. This behaviour might be explained by thermal mismatch between the NiCr matrix and CrC particles, generating new dislocations during cooling from the heat treatment temperature. Phase transformations or partial dissolution and reprecipitation of carbides could also introduce new dislocations due to volume changes and lattice mismatches [32]. The presence of two phases with different thermal properties can lead to the development of internal stresses, further contributing to dislocation generation [33].

The observed increase in microstrain is consistent with the rise in dislocation density, as microstrain is often directly related to the presence of lattice defects. The formation of new phases or changes in existing phases during heat treatment could lead to local lattice distortions, increasing overall microstrain. These observations suggest that the heat treatment is causing modifications to the alloy's structure, possibly involving precipitation, phase transformations, and thermal stress effects. The simultaneous decrease in crystallite size and increases in dislocation density and microstrain indicate a delicate balance between competing mechanisms of microstructural evolution.

It is worth noting that similar complex behaviours have been observed in other alloy systems. For instance, in some high-entropy alloys, particle size effects have been shown to significantly influence dislocation density, microstructure, and phase transformations [34]. In aluminium alloys, solution heat treatment can lead to significant changes in grain size, precipitate distribution, and consequently, mechanical properties [35].

The heat treatment of Cr_3C_2-NiCr coatings results in a complex interplay of phase transformations, precipitation phenomena, and structural refinements. The formation of new carbide phases, such as $Cr_{23}C_6$, along with the observed changes in crystallite size, microstrain, and dislocation density, highlight the dynamic nature of these coatings under thermal exposure. The refinement of the microstructure and such temperature-induced changes are expected to impact the coating's corrosion resistance, which is explored in the following sections.

3.2. Electrochemical Impedance Spectroscopy

Electrochemical impedance spectroscopy (EIS) was undertaken for each sample under a three-electrode setup, with artificial seawater as the solution medium. The results from the EIS are shown in Figures 10 and 11.

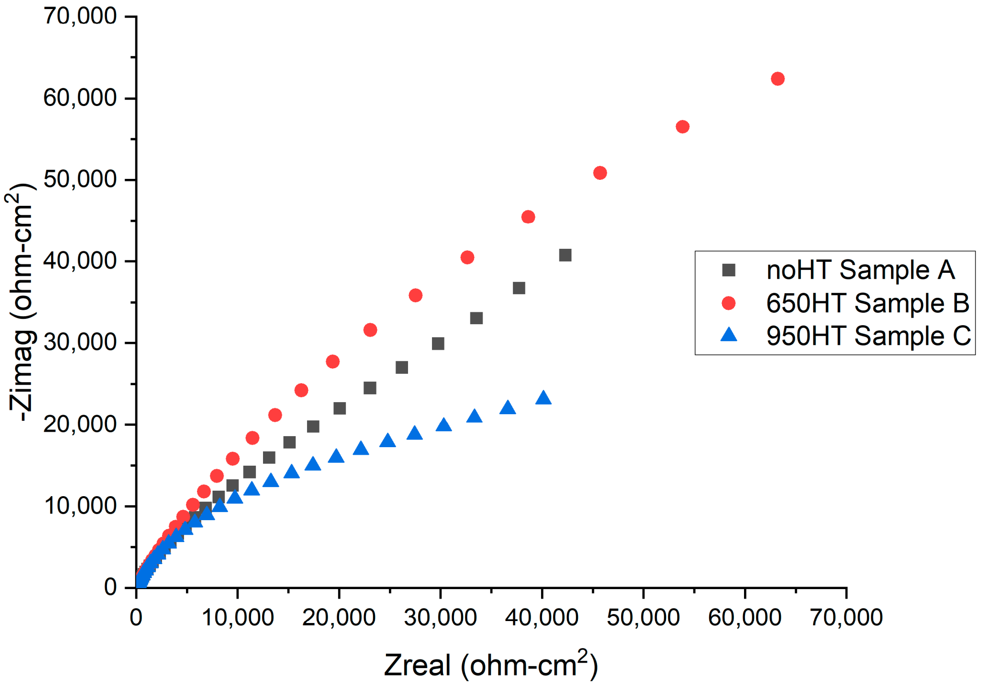

Figure 10. EIS Nyquist plot for Samples A, B, and C.

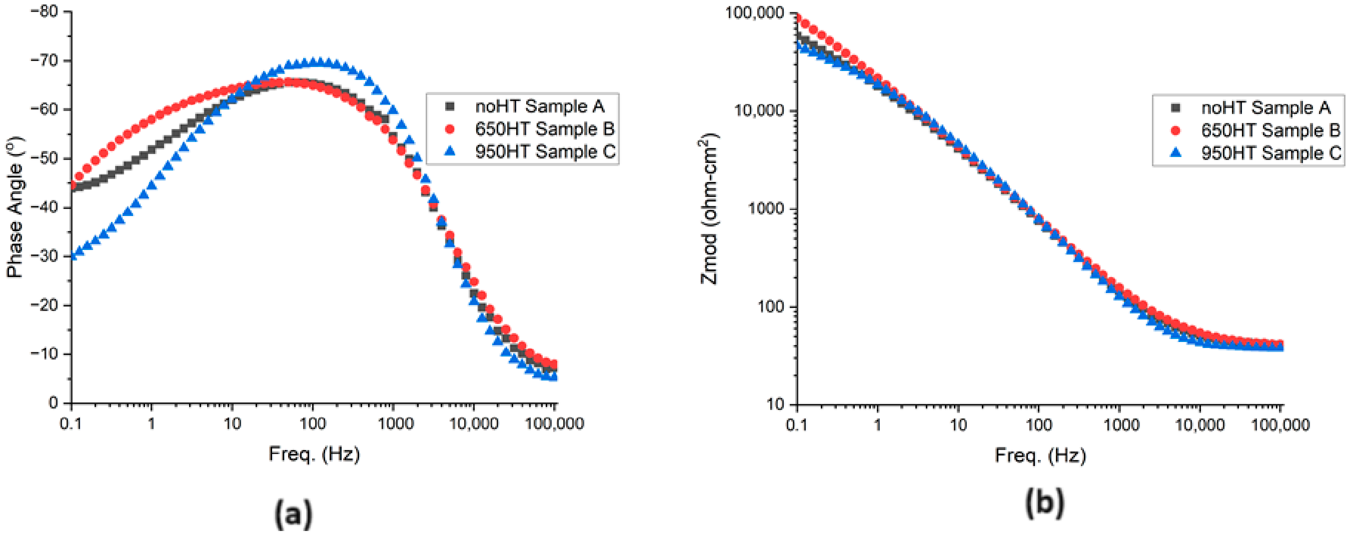

Figure 11. Bode plots: (**a**) phase vs. freq and (**b**) Mod Z vs. freq.

Results from the EIS data can be modelled to equivalent circuit models in order to gauge their behaviour. For coatings, this is expected to follow the double layer model $R_{soln}[C_c[R_{po}[C_{cor}R_{cor}]]]$ as shown in Figure 12 [36].

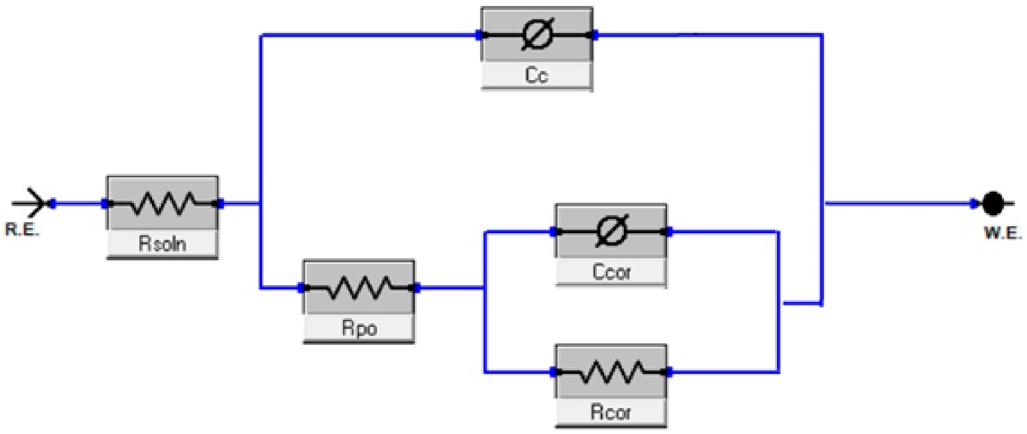

Figure 12. Equivalent circuit model for the coating system.

In this model, R_{soln} indicates solution resistance, R_{po} represents porous resistance of the coating, C_c represents coating capacitance, C_{cor} represents the double layer capacitance, and R_{cor} represents charge transfer resistance [36]. With this model, it was also found that the system was better represented by replacing the capacitors with constant phase elements (Q), which may be due to non-homogeneity within the system such as that due to imperfect coatings. As such, the representation parameters obtained from modelling this system are shown in Table 10.

Table 10. EIS parameters obtained from equivalent circuit modelling.

Sample	**R_{soln} (Ω)**	**Q_c ($\Omega^{-1}cm^{-2}s^n$)**	**n_c**	**R_{po} (Ω)**	**Q_{cor} ($\Omega^{-1}cm^{-2}s^n$)**	**n_{cor}**	**R_{cor} (Ω)**	**Chi^2**
noHT Sample A	39.79	8.89×10^{-6}	0.7763	1.90×10^{4}	1.75×10^{-5}	0.4203	4.61×10^{5}	1.57×10^{-4}
650HT Sample B	39.76	9.86×10^{-6}	0.754	2.77×10^{4}	7.11×10^{-6}	0.2993	1.37×10^{6}	2.44×10^{-4}
950HT Sample C	37.00	4.88×10^{-6}	0.8554	0.01371	1.93×10^{-5}	0.2616	3.03×10^{5}	8.12×10^{-5}

Chi-squared values found from these models were all less than 10^{-3}, indicating a high quality of fit towards the data.

The electrochemical impedance spectroscopy (EIS) results for the heat-treated NiCr-CrC coatings reveal significant differences in corrosion behaviour among the samples, providing valuable insights into the effects of heat treatment on the coating's microstructure and electrochemical properties. The Nyquist plot (Figure 10) shows distinct semicircular arcs for each sample, with the 650 °C heat-treated sample (Sample B) exhibiting the largest arc diameter, followed by the non-heat-treated sample (Sample A), and the 950 °C heat-treated sample (Sample C) showing the smallest arc. This trend is consistent with the charge transfer resistance (Rcor) values extracted from the equivalent circuit modelling (Table 10), where Sample B demonstrates the highest Rcor (1.37×10^6 Ω), indicating superior corrosion resistance compared to Samples A (4.61×10^5 Ω) and C (3.03×10^5 Ω). The observed differences in corrosion behaviour can be attributed to microstructural changes induced by heat treatment. At 650 °C, the coating likely undergoes beneficial transformations that enhance its protective properties. This temperature may promote the formation of a more compact and homogeneous microstructure, potentially through the reduction in porosity and the redistribution of chromium carbides. The increased Rcor for Sample B suggests the formation of a more stable passive layer, which acts as a barrier against corrosive species. Conversely, the 950 °C heat treatment (Sample C) appears to have a detrimental effect on the coating's corrosion resistance.

The non-heat-treated sample (A) shows intermediate performance, suggesting that while the as-sprayed coating provides some corrosion protection, it can be further improved through optimised heat treatment. The capacitance values (Qc and Qcor) provide additional insights into the coating's properties. Sample C exhibits the lowest Qc ($4.88 \times 10^{-6}\ \Omega^{-1}\text{cm}^{-2}\text{s}^{\text{n}}$), which might indicate a thicker oxide layer with respect to specific phases or altered dielectric properties due to the high-temperature treatment. However, its higher Qcor ($1.93 \times 10^{-5}\ \Omega^{-1}\text{cm}^{-2}\text{s}^{\text{n}}$) suggests increased surface area at the coating/electrolyte interface, consistent with the observed high porosity.

These EIS results align with findings from previous studies on heat-treated Cr_3C_2-NiCr coatings. For instance, Matthews et al. observed that heat treatment at moderate temperatures (500–700 °C) led to beneficial microstructural changes, including carbide precipitation and matrix densification, which improved corrosion resistance [37]. However, treatments at higher temperatures (>800 °C) resulted in excessive carbide coarsening and potential chromium depletion in the matrix, compromising the coating's protective properties [28]. Primarily, excessive carbide dissolution occurs at this elevated temperature, where chromium carbides may dissolve into the matrix. This process can potentially create new pores or channels within the coating structure, leading to a more interconnected pore network. Such interconnectivity facilitates easier electrolyte penetration, despite the overall reduction in total porosity.

Figure 11a shows the Bode plot (phase angle vs. frequency) observed for the three samples. The behaviour in the low-frequency regime is particularly important as it relates to the electrochemical processes occurring at the electrode/electrolyte interface. In the low-frequency region, Sample B (650 °C heat-treated) exhibits a higher phase angle of 45° at 0.1 Hz, indicating superior corrosion resistance and suggesting formation of a more stable, protective passive film. This aligns with the optimised microstructure observed in the SEM analysis, where the balanced carbide size (138 μm^2) and increased $Cr_{23}C_6$ content (13.9%) potentially contribute to enhanced passivation behaviour.

Conversely, Sample C (950 °C heat-treated) shows the lowest phase angle of 30° at very low frequencies (0.1 Hz), implying that despite improved homogeneity, the 950 °C treatment may result in a less effective corrosion barrier. This could be attributed to the excessive carbide dissolution (carbide size reduced to 98.7 μm^2). In the mid-frequency range at about 80–100 Hz, all samples show a continued increase in phase angle. Sample C exhibits the steepest rise, overtaking Sample A around 10 Hz and reaching the highest peak around 100 Hz. Sample B maintains a relatively steady increase, reaching its peak at a slightly higher frequency than Sample C. Sample A shows the least pronounced peak in this region.

The behaviour in the mid-frequency range often relates to the properties of the coating itself, including its porosity and overall integrity. The steeper rise and higher peak of Sample C could indicate that the high-temperature treatment at 950 °C likely led to the formation of new interfaces within the coating microstructure. These interfaces could be between different phases or at grain boundaries. The sharp peak at 100 Hz may represent the charge transfer processes occurring at these newly formed interfaces. According to recent research on Ni-Cr alloys, high-temperature treatments can lead to the formation of complex oxide layers with distinct interfaces between metal/inner oxide and inner oxide/outer oxide layers [38]. The charge transfer across these interfaces could contribute to the observed peak. The peak also indicates a time constant typically associated with another specific electrochemical process [39]. This peak suggests improved coating homogeneity, attributable to significant carbide size reduction (98.7 μm^2) and increased matrix Cr content (20.6 wt%) as observed in microstructural characterisation. These changes likely created new diffusion pathways within the coating. The peak at 100 Hz could represent the characteristic frequency of ion diffusion through these modified pathways, as due to the lowest pore resistance compared to other samples as observed in Table 9. Sample B's moderate but steady response indicates a balanced microstructure combining good coating integrity with optimal passive film properties. Sample B's optimised carbide size and distribution likely contribute to its favourable electrochemical impedance response [40]. Sample A lacks such a pronounced peak, suggesting a more homogeneous electrochemical response, potentially indicating a uniform passive film compared to Sample C, with higher overall corrosion resistance as observed in Table 9.

In the high-frequency range (>1000 Hz), all samples converge towards lower phase angles, approaching purely resistive behaviour, typical in electrochemical systems and representing electrolyte resistance response [39]. This convergence indicates similar bulk electrolyte properties for all samples. However, subtle differences in approaching this convergence point can provide information about coating pore resistance and capacitance.

Figure 11b shows the Bode plot displaying the modulus of impedance (|Z|) versus frequency on a logarithmic scale for all three samples. At low frequencies (0.1–1 Hz), the impedance values provide information about the overall corrosion resistance of the coating system. In this region, we observe that the 650 °C heat-treated sample (red line) exhibits the highest impedance, followed by the 950 °C heat-treated sample (blue line), and lastly, the non-heat-treated sample (black line). This trend suggests that heat treatment, particularly at 650 °C, enhanced the corrosion resistance of the coating. The higher impedance of the 650 °C heat-treated sample indicates a more effective barrier against corrosive species, which could be attributed to microstructural changes induced by the heat treatment. Previous studies have shown that moderate heat treatment temperatures can lead to the formation of beneficial phases and improved coating densification [41]. The enhanced corrosion resistance at 650 °C may be due to the optimal balance between carbide dissolution and matrix phase transformation, resulting in a more homogeneous and protective coating structure. Furthermore, the behaviour in the low- to mid-frequency range provides insights into the properties of the electrochemical double layer at the coating/electrolyte interface. The higher impedance of the 650 °C sample indicates a more effective barrier against charge transfer processes, which is crucial for long-term corrosion protection [39].

3.3. Corrosion Evaluation

3.3.1. Potentiodynamic Results

Potentiodynamic tests were conducted by exposing the samples in a three-electrode setup to artificial seawater at a neutral pH of 7. The results are shown in Figure 13.

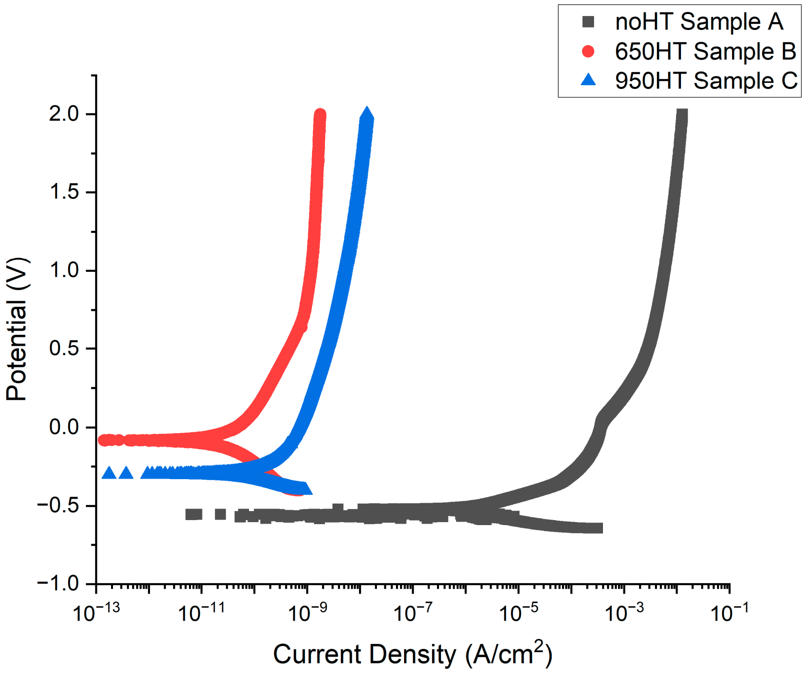

Figure 13. Potentiodynamic curves for Samples A, B, and C.

Figure 10 presents the potentiodynamic polarisation curves for Samples A, B, and C, illustrating the differences in corrosion behaviour between the non-heat-treated sample and those heat-treated at 650 °C and 950 °C, respectively. The potentiodynamic polarisation curves provide valuable insights into the corrosion behaviour of the NiCr-CrC coatings subjected to different heat treatments.

Using Tafel plot analysis from Gamry Echem Analyst software, I_{corr} and E_{corr} can also be found to further validate the visual analysis as well as the values of E_{OC}. These are reported in Table 11.

Table 11. Corrosion parameters generated from Tafel analysis.

Variable	Sample A (noHT)	Sample B (650HT)	Sample C (950HT)
E_{OC}	−550	−95	−305
E_{corr} (mV)	−564.2	−79.9	−297
I_{corr} (A/cm^2)	4.54×10^{-6}	6.5×10^{-11}	1.7×10^{-10}

The sample heat-treated at 650 °C (Sample B) demonstrates superior corrosion resistance compared to the sample heat-treated at 950 °C (Sample C) and the non-heat-treated sample (Sample A). Sample B exhibits the most favourable characteristics, having the most positive Ecorr of −79.9 mV, indicating the slowest corrosion rate, as well as the lowest Icorr value of 6.5×10^{-11} A/cm^2.

These features indicate that the 650 °C heat treatment optimised the microstructure of the NiCr-CrC coating, resulting in enhanced corrosion resistance. The wide passive region suggests the formation of a stable and protective passive film. The heat treatment process at 650 °C is crucial in promoting the formation of passivity on the surface of NiCr-CrC coatings, leading to a significant improvement in their corrosion behaviour. This enhancement in passivation behaviour is attributed to the transformation of the coatings into a crystalline structure, particularly rich in chromium oxides, which contributes to the coatings' ability to resist corrosion and passivate the surface effectively [28]. Furthermore, the heat treatment process induces microstructural changes in the coatings, such as the transformation of the amorphous phase into a nanocrystalline structure, which further strengthens the coatings and enhances their mechanical properties [42]. The formation of these passive layers on the surface of the coatings after heat treatment at 650 °C enhances their resistance to aggressive environments by providing a protective barrier against corrosive elements. The presence of these oxide layers alters the surface chemistry of the coatings, improving their passivation behaviour and overall corrosion resistance [28].

The sample heat-treated at 950 °C (Sample C) shows intermediate corrosion resistance. It has a lower corrosion potential of approximately −0.25 V, and an average passive current of about 4×10^{-9} A/cm^2. The data from Table 11 support this observation, showing Sample C with an intermediate E_{corr} of −297 mV, significantly lower than that of Sample B and higher than that of Sample C. While this sample performs better than the non-heat-treated sample, it is not as effective as the 650 °C treatment. Excessive heat treatment temperatures exceeding 900 °C in NiCr-CrC coatings have been found to have detrimental effects on the microstructure of the coatings. Such microstructural changes compromise the coating's ability to form a stable passive film, ultimately resulting in reduced corrosion resistance. Specifically, at 950 °C, there is a risk of partial dissolution, which can diminish the effectiveness of carbide dispersion in enhancing corrosion resistance [21]. This dissolution can be seen in SEM imagery such as in Figure 3.

The non-heat-treated sample (Sample A) of NiCr-CrC coatings demonstrates inferior corrosion resistance, characterised by a low corrosion potential of approximately −0.50 V, and an average passive current density of 4×10^{-3} A/cm^2. This inferior corrosion resistance is further evidenced with Sample A having the most negative Ecorr of −564.2 mV and the highest Icorr of 4.54×10^{-6} A/cm^2, indicating the fastest corrosion rate among the three samples, as shown in Table 10. This lower corrosion resistance behaviour in the non-heat-treated sample can be attributed to the as-sprayed microstructure, which typically contains residual stresses, porosity, and a non-uniform distribution of phases.

The exceptional performance of the 650 °C heat-treated sample in NiCr-CrC coatings can also be attributed to phase transformations and diffusion processes facilitated by this specific heat treatment temperature. It is well expected that there is sufficient atomic mobility to allow for the redistribution of alloying elements and the formation of beneficial phases within the coatings without inducing excessive grain growth or unwanted precipitations. It also facilitates achieving a microstructure with optimised carbide distribution and matrix refinement. Research has shown that heat treatment promotes the formation of fine, evenly distributed $Cr_{23}C_6$ carbides within the coatings, which act as effective barriers against corrosion [28]. Moreover, the 650 °C heat treatment likely strikes an optimal balance in terms of residual stress relief. Moderate heat treatment temperatures have been shown to effectively reduce residual stresses in cold-sprayed coatings without causing thermal damage or compromising the integrity of the coating/substrate interface. This stress relief mechanism plays a crucial role in enhancing corrosion resistance by minimising the likelihood of microcrack formation and enhancing the overall cohesion of the coating [43].

3.3.2. Potentiostatic Tests and Characterisation

Using the potentiodynamic plots as a guide, potentiostatic points can be chosen for testing to investigate any changes on the surface. For all three samples, a potentiostatic point of 2.0V was chosen due to being the final point swept during the potentiodynamic test. Additionally, a potentiostatic point of 45 mV was chosen for the noHT Sample A to reflect the point of inflection on the potentiodynamic plot.

Optical microscopy results of potentiostatic points taken after initial as-polished state are shown in Figures 14–17.

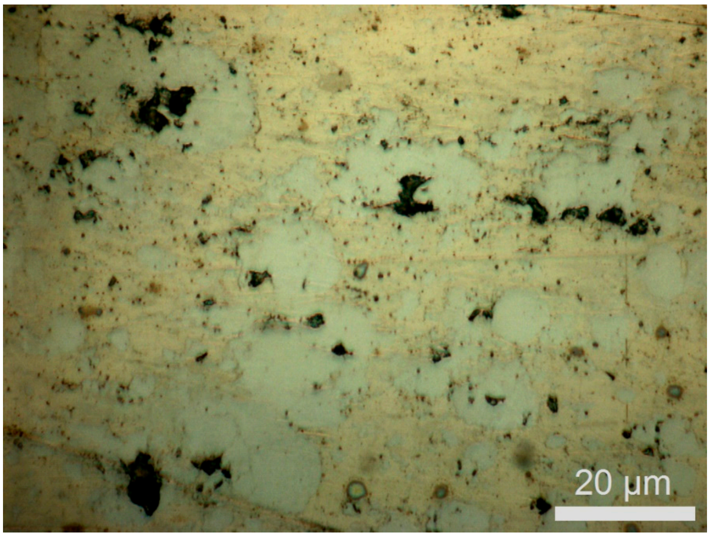

Figure 14. Optical microscopy for the noHT Sample A's potentiostatic point at 45 mV.

From the optical imagery in Figure 14, it appears that holding the noHT Sample A surface at 45 mV does not significantly affect its characteristics compared to its non-corroded state. However, testing at 2.0 V for the noHT Sample A showed significant damage to the matrix, whilst the carbides appeared to mainly remain intact, as seen in Figure 15. This is in contrast to the heat-treated samples, where testing the 2.0 V potentiostatic point did not appear to yield significant damage to the surface, as seen in Figures 16 and 17.

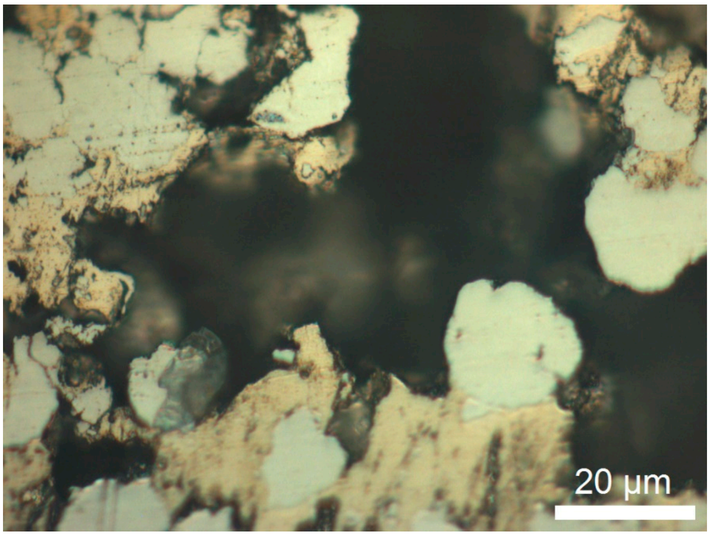

Figure 15. Optical microscopy for the noHT Sample A's potentiostatic point at 2000 mV.

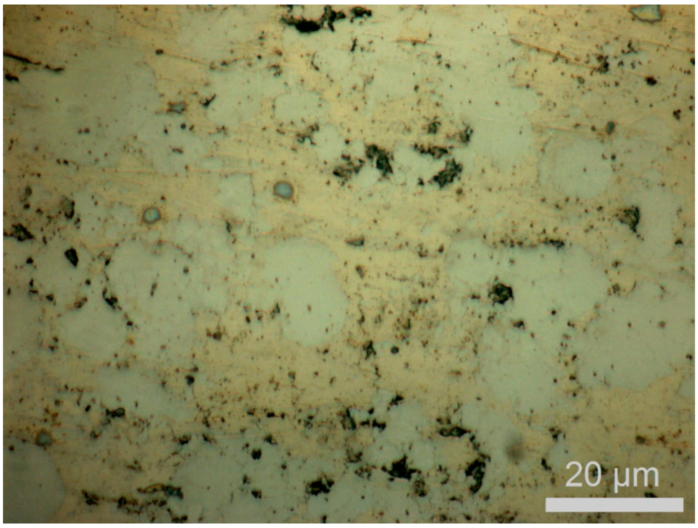

Figure 16. Optical microscopy for the 650HT Sample B's potentiostatic point at 2000 mV.

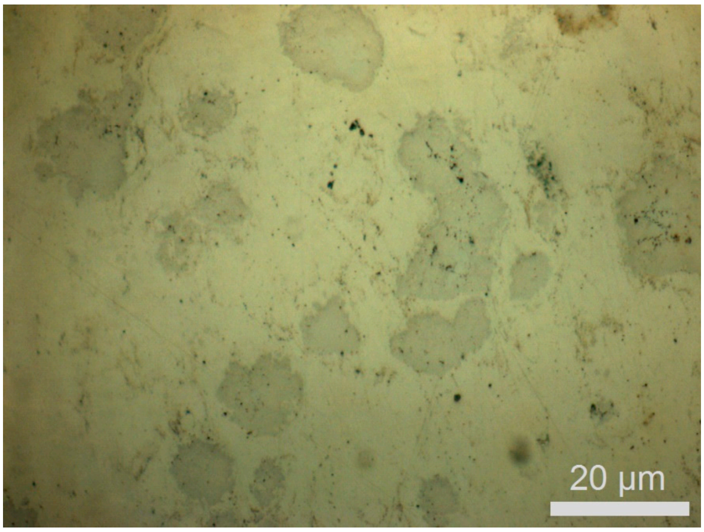

Figure 17. Optical microscopy for the 950HT Sample C's potentiostatic point at 2000 mV.

Chemical composition analysis of the corroded surfaces after being held at the 2.0 V potentiostatic point was conducted via EDS, and the results are provided in Tables 12 and 13.

Table 12. Matrix post-corrosion sample compositions via EDS (wt%).

Label	C	Cr	Ni	Total
Sample A (noHT)	2.2	5.3	92.7	100
Sample B (HT 650 °C)	1.80	10.8	87.4	100
Sample C (HT 950 °C)	1.2	13.4	85.4	100

Table 13. Carbide post-corrosion sample compositions via EDS (wt%).

Label	C	Cr	Ni	Si	Total
Sample A (noHT)	3.2	81.0	14.8	0.8	100
Sample B (HT 650 °C)	2.30	82.3	14.6	0.5	100
Sample C (HT 950 °C)	4.2	77.6	17.6	0.6	100

Notably, as per Tables 7 and 12, the proportion of chromium content in the matrix decreased after corrosion for Samples A and C (7.9 wt%to5.3 wt% and 20.6 wt%to13.4 wt% for Samples A and C, respectively). However, the chromium content within the matrix for the 650HT Sample B remained approximately consistent (10.5 wt%to10.8 wt%), which could potentially be attributable to it having the highest resistance towards corrosion, as seen in previous potentiodynamic and EIS results.

3.4. Hardness Tests

A comparison of hardness from both the uncorroded samples and after holding at a potentiostatic point of 2.0 V can be seen in the following table, Table 14.

Table 14. Hardness of samples.

	As-Sprayed Hardness ± 1σ ($HV_{0.1}$)	Post-Corrosion Hardness ± 1σ ($HV_{0.1}$)
Sample A carbide	1145 ± 40.3	506 ± 4.0
Sample B carbide	800 ± 43.2	475 ± 21.7
Sample C carbide	646 * ± 378	402 * ± 213.3
Sample A matrix	235 ± 14.8	237 ± 15.7
Sample B matrix	192 ± 20.5	189 ± 5.2
Sample C matrix	164 ± 14.6	176 ± 23.2

* Explained in following section.

It can be seen that the hardness of carbides was significantly compromised by the corrosion tests for all samples (i.e., 1145HV to 506HV for the noHT Sample A and 800HV to 475HV for the 650HT Sample B). Interestingly, it can be noted that the hardness results for the 950HT Sample C could not be reliably taken. Whilst some "normal" square indentations were sometimes produced, carbides would sometimes also display visible collapse around the indentation (Figure 18) or even punching in/removing of carbides entirely after indentation (Figure 19), suggesting a compromise in the heat-treated carbides beyond that affecting Samples A and B. This would suggest a loose attachment of carbides to the matrix for samples heat-treated at 950 °C.

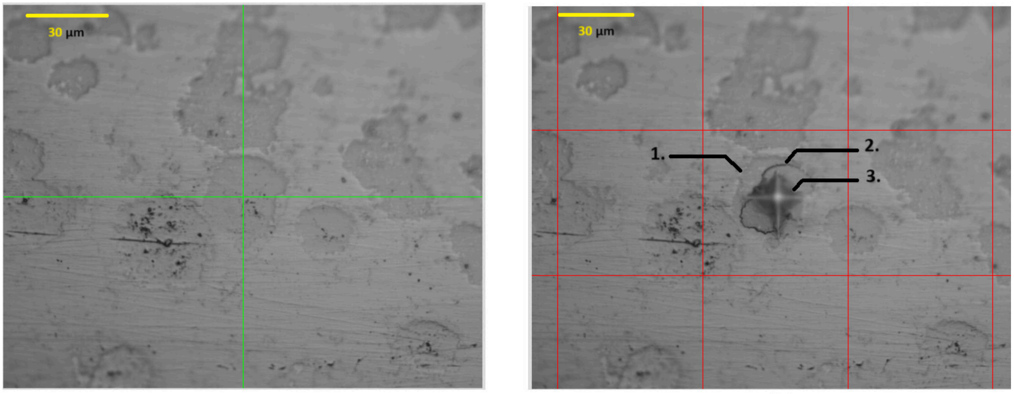

(a) (b)

Figure 18. Hardness tests for 950HT Sample C (**a**) before indentation and (**b**) after indentation. Also note the following features: 1. carbides, 2. collapse of carbide around the indentation, and 3. the square indentation itself.

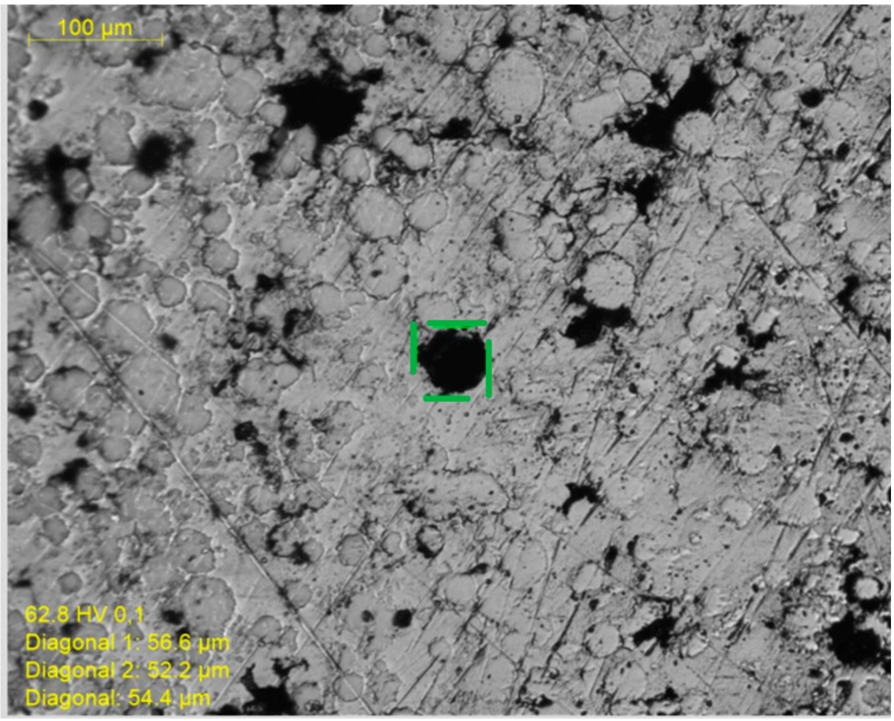

Figure 19. Complete removal of carbide post-indentation, as shown surrounded by green box.

By contrast, the matrix for Samples A–C did not significantly decrease post-corrosion. In fact, hardness values increased slightly post-corrosion for Sample A (235 to 237HV) and Sample C (164 to176HV).

4. Discussion

When the agglomerated powder containing NiC-CrC is sprayed at high speeds onto a substrate, there is deformation of the NiCr powder and sometimes disintegration of the brittle carbide particles. There is also incomplete bonding, and voids are present in the coating. Due to the incomplete bonding nature of the powder particles, the X-ray diffraction results show the lowest dislocation density. As the samples get heat-treated, there is good bonding between the powder particles, thus forming a more solid material. This then increases the dislocation density of the coating. Increasing the heat treatment temperature from 650 to 950 °C increases the carbide dissolution, and this has been observed before for stainless steels [17]. The accommodation of the phase transformation and dissolution produces lattice strains that increase the dislocation density of the coating. The total number of carbides decreased with increasing heat treatment temperature, as shown in Table 5. The heat treatment also changed the chromium distribution in the coating, as shown in Tables 7 and 8. The matrix composition of chromium increased from 7.9% in the as-sprayed sample to 20.6% for the 950 °C heat-treated sample. This likely resulted in galvanic corrosion of the interface between the carbides and the matrix. This effect was seen in the loosening of the carbides during the potentiodynamic test. The matrix fully corroded in the potentiodynamic test due to lower chromium content of 7.9% in the matrix compared to 86.6% chromium in the carbides. This resulted in the dissolution of the matrix, which pointed to the possibility that the matrix dissolves in preference to the carbides.

Further, with heat treatment, the carbides themselves started to dissolve, increasing the carbon and chromium contents in the matrix. The dissolution introduced more interfaces between the carbides and the matrix, resulting in poorer corrosion resistance for the sample heat-treated at 950 °C. However, not only did heat treatment at 650 °C reduce the porosity and consolidate the bonding between powder particles, but the interface corrosion between the carbides and the matrix was not so severe as to dislodge the carbides. Interestingly, this investigation could not identify the presence of oxides, which other investigators found [44]. The presence of oxides would result in further disintegration of carbides, as the chromium should become free from the carbides to form the oxides. Based on this, the following mechanism is presented.

The SEM images reveal significant microstructural changes in the Cr_3C_2-NiCr coatings after different heat treatments, providing crucial insights into their corrosion behaviour. An illustrated explanation for this behaviour is shown in Figure 20.

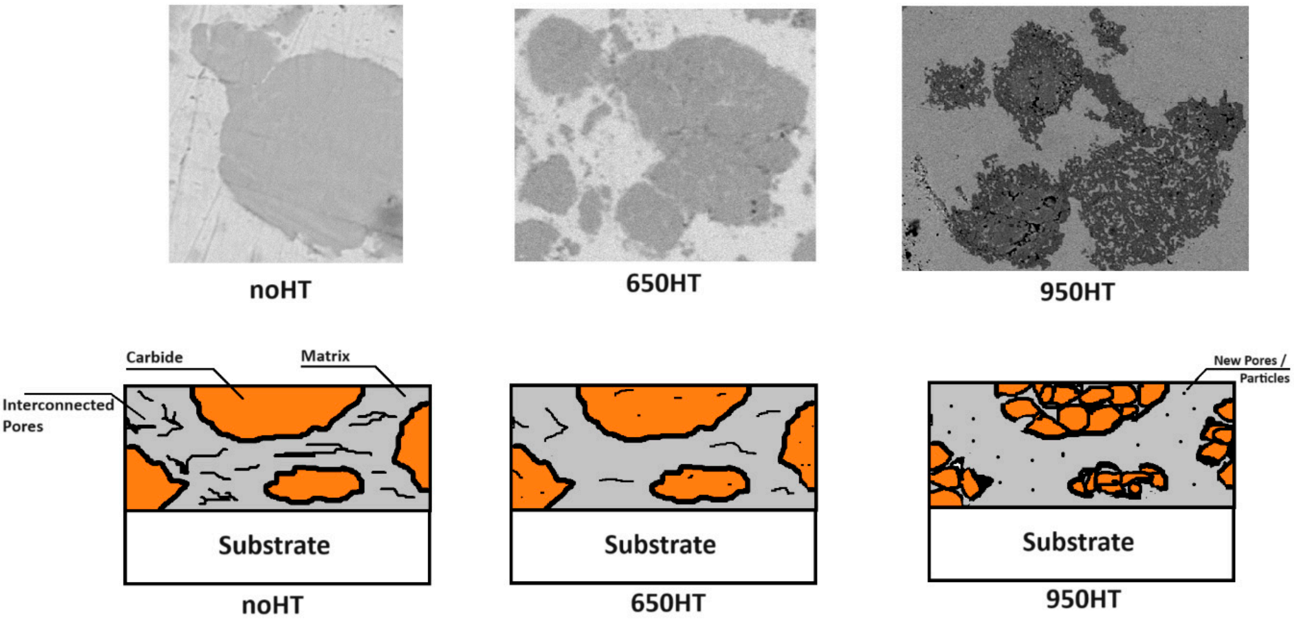

Figure 20. Illustrated microstructural changes with heat treatment.

The non-heat-treated (noHT) sample shows distinct, well-defined carbide particles embedded in the NiCr matrix. This heterogeneous structure, typical of the as-sprayed condition, likely contributes to the observed galvanic corrosion with preferential matrix removal, as evidenced by the electrochemical tests. The 650 °C heat-treated sample exhibits a more refined microstructure. The carbides appear slightly less defined compared to the noHT sample, suggesting the onset of carbide dissolution and potential formation of $Cr_{23}C_6$, corroborated by the XRD data showing 13.9% $Cr_{23}C_6$ content. This microstructural refinement correlates well with the superior corrosion resistance observed, including the highest corrosion potential and widest passive region.

The 950 °C heat-treated sample shows significant carbide decomposition, resulting in greater interface between carbides and the matrix. There was also greater dislocation density due to trying to accommodate the new interfaces due to carbide dissolution. The galvanic couple developed, due to the increase in the chromium content in the matrix, between the carbide and the matrix. This resulted in dissolution at the interface between the matrix and the carbide.

The observed microstructural evolution provides a mechanistic explanation for the varying corrosion behaviours. The 650 °C heat treatment strikes an optimal balance between beneficial microstructural refinement and preservation of coating integrity, resulting in enhanced corrosion resistance. In contrast, while the 950 °C treatment leads to extensive carbide decomposition and increased matrix Cr content, the excess porosity significantly compromises its corrosion resistance. This porosity likely provides pathways for corrosive media to penetrate the coating, offsetting any potential benefits from increased chromium in the matrix.

5. Conclusions

This study provides valuable insights into the effects of heat treatment on the microstructure, corrosion behaviour, and mechanical properties of cold-sprayed Cr_3C_2-NiCr coatings. The investigation revealed that post-deposition heat treatment significantly influences the coating’s performance, with the optimal temperature identified as 650 °C. The sample heat-treated at 650 °C exhibited superior corrosion properties, including the highest corrosion potential (-79.9 mV) and largest charge transfer resistance (1.37×10^6 Ω). This improved performance can be attributed to the formation of a more stable and protective passive film, optimal carbide dissolution, and a homogeneous microstructure. In contrast, heat treatment at 950 °C, while reducing porosity, led to excessive carbide dissolution and potential chromium depletion in the matrix. This resulted in intermediate corrosion resistance, inferior to the 650 °C treatment but still better than the as-sprayed condition. The non-heat-treated sample displayed the poorest corrosion resistance, characterised by galvanic corrosion and preferential matrix removal. Mechanical property changes were also observed, with carbide hardness significantly decreasing after corrosion testing, particularly in the as-sprayed and 650 °C heat-treated samples. The 950 °C heat-treated sample showed unreliable carbide hardness measurements, indicating compromised structural integrity. These findings highlight the critical role of controlled heat treatment in optimising the performance of cold-sprayed Cr_3C_2-NiCr coatings. This study demonstrates that achieving superior corrosion resistance requires a delicate balance between microstructural refinement, phase transformations, and preservation of coating integrity.

Author Contributions: Conceptualisation, K.K. and C.T.; methodology, K.K. and C.T.; validation, C.T.; formal analysis, C.T.; investigation, C.T.; writing—original draft preparation, C.T. and N.K.E.; writing—review and editing, C.T., K.K., and N.K.E.; supervision, K.K. and N.K.E. All authors have read and agreed to the published version of the manuscript.

Funding: This research was supported by Australian Government Research Training Program Scholarship through Charles Darwin University.

Data Availability Statement: The original contributions presented in the study are included in the article material, further inquiries can be directed to the corresponding author.

Acknowledgments: The authors would like to acknowledge Spee3D for their help in preparing samples. Cedric Tan was supported by the Australian Government Research Training Program Scholarship through Charles Darwin University.

Conflicts of Interest: The authors declare no conflict of interest.

References

1. Sun, W.; Chu, X.; Lan, H.; Huang, R.; Huang, J.; Xie, Y.; Huang, G. Huang Current implementation status of cold spray technology: A short review. *J. Therm. Spray Technol.* **2022**, *31*, 848–865. [CrossRef] [PubMed]
2. Kumar, S.; Kumar, M.; Jindal, N. Overview of cold spray coatings applications and comparisons: A critical review. *World J. Eng.* **2020**, *17*, 27–51. [CrossRef]
3. Moridi, A.; Hassani-Gangaraj, S.M.; Guagliano, M.; Dao, M. Cold spray coating: Review of material systems and future perspectives. *Surf. Eng.* **2014**, *30*, 369–395. [CrossRef]
4. Srikanth, A.; Basha, G.M.T.; Venkateshwarlu, B. A brief review on cold spray coating process. *Mater. Today Proc.* **2020**, *22*, 1390–1397. [CrossRef]
5. Nelson, G. The Influence of Microstructure on the Corrosion and Wear Mechanisms Of High Chromium White Irons in Highly Caustic Solutions. Ph.D. Thesis, School of Mechanical Engineering The University of Adelaide, Adelaide, Australia, December 2010.
6. Champagne, V.; Widener, C.; Nardi, A.; Ferguson, G. Structural Repair for Stryker HH Steel Body Panels Using Cold Spray. In Proceedings of the Ground Vehicle Systems Engineering and Technology Symposium. In Proceedings of the 2019 NDIA Ground Vehicle Systems Engineering And Technology Symposium, Novi, MI, USA, 13–15 August 2019.
7. Singh, H.; Kumar, M.; Singh, R. An overview of various applications of cold spray coating process. *Mater. Today Proc.* **2022**, *56*, 2826–2830. [CrossRef]
8. Zikin, A.; Hussainova, I.; Katsich, C.; Badisch, E.; Tomastik, C. Advanced chromium carbide-based hardfacings. *Surf. Coat. Technol.* **2012**, *206*, 4270–4278. [CrossRef]
9. Antonov, M.; Hussainova, I.; Veinthal, R.; Pirso, J. Effect of temperature and load on three-body abrasion of cermets and steel. *Tribol. Int.* **2012**, *46*, 261–268. [CrossRef]
10. Gupta, N.; Singh, S.K.; Pandey, S.M. Tribological characterisation of thermal sprayed CrC alloyed coating–A review. *Adv. Mater. Process. Technol.* **2021**, *7*, 660–683. [CrossRef]
11. Forouzan, F.; Guitar, M.A.; Vuorinen, E.; Mücklich, F. Effect of carbon partitioning, carbide precipitation, and grain size on brittle fracture of ultra-high-strength, low-carbon steel after welding by a quenching and partitioning process. *Metals* **2018**, *8*, 747. [CrossRef]
12. Mendez, P.F.; Barnes, N.; Bell, K.; Borle, S.D.; Gajapathi, S.S.; Guest, S.D.; Izadi, H.; Gol, A.K.; Wood, G. Welding processes for wear resistant overlays. *J. Manuf. Process.* **2014**, *16*, 4–25. [CrossRef]
13. Guilemany, J.; Miguel, J.; Vizcaıno, S.; Lorenzana, C.; Delgado, J.; Sanchez, J. Role of heat treatments in the improvement of the sliding wear properties of Cr3C2–NiCr coatings. *Surf. Coat. Technol.* **2002**, *157*, 207–213. [CrossRef]
14. Matthews, S.; Hyland, M.; James, B. Microhardness variation in relation to carbide development in heat treated Cr3C2–NiCr thermal spray coatings. *Acta Mater.* **2003**, *51*, 4267–4277. [CrossRef]
15. Fernandez, R.; Jodoin, B. Effect of particle morphology on cold spray deposition of chromium carbide-nickel chromium cermet powders. *J. Therm. Spray Technol.* **2017**, *26*, 1356–1380. [CrossRef]
16. Sun, W.; Tan, A.W.-Y.; Wu, K.; Yin, S.; Yang, X.; Marinescu, I.; Liu, E. Post-process treatments on supersonic cold sprayed coatings: A review. *Coatings* **2020**, *10*, 123. [CrossRef]
17. Govande, A.R.; Chandak, A.; Sunil, B.R.; Dumpala, R. Carbide-based thermal spray coatings: A review on performance characteristics and post-treatment. *Int. J. Refract. Met. Hard Mater.* **2022**, *103*, 105772. [CrossRef]
18. Clark, J.N.; Glasson, D.R.; Jayaweera, S.A.A. Oxidation of chromium carbide. *Thermochim. Acta* **1986**, *103*, 193–199. [CrossRef]
19. Fontana, M.G. *Corrosion Engineering*, 3rd ed.; McGraw-Hill: New York, NY, USA, 1986.
20. Nam, T.-H.; An, E.; Kim, B.J.; Shin, S.; Ko, W.-S.; Park, N.; Kang, N.; Jeon, J.B. Effect of post weld heat treatment on the microstructure and mechanical properties of a submerged-arc-welded 304 stainless steel. *Metals* **2018**, *8*, 26. [CrossRef]
21. Suegama, P.; Espallargas, N.; Guilemany, J.M.; Fernández, J.; Benedetti, A.V. Electrochemical and structural characterization of heat-treated Cr3C2–NiCr coatings. *J. Electrochem. Soc.* **2006**, *153*, B434. [CrossRef]
22. Bala, N.; Singh, H.; Prakash, S. Accelerated hot corrosion studies of cold spray Ni–50Cr coating on boiler steels. *Mater. Des.* **2010**, *31*, 244–253. [CrossRef]
23. Drozdz, M.; Kyzlol, K.; Grzesik, Z. Chromium-based oxidation-resistant coatings for the protection of engine valves in automotive vehicles. *Mater. Tehnol.* **2017**, *51*, 603–607. [CrossRef]
24. Smola, G.; Gawel, R.; Kyziol, K.; Miszczak, M.; Grzesik, Z. Influence of nickel on the oxidation resistance at high temperatures of thin chromium coatings. *Oxid. Met.* **2019**, *91*, 625–640. [CrossRef]
25. Powdersondemand. WIP-C2 Datasheet. 2024. Available online: https://order.powdersondemand.com/powders/WIP-C2 (accessed on 11 May 2024).
26. Munteanu, C.; Chicet, D.-L.; Istrate, B.; Stefan, A.; Vida-Simiti, I. Influence of deposition technology on the morphology of chromium carbide-based powder coatings. *J. Eng. Sci. Innov.* **2024**, *9*, 33–46.
27. Spee3D. SPEE3D 3D Metal Printing | Fast & Affordable Metal Parts. 2019. Available online: https://www.spee3d.com/ (accessed on 2 February 2024).
28. Matthews, S.; James, B.; Hyland, M. The role of microstructure in the high temperature oxidation mechanism of Cr3C2–NiCr composite coatings. *Corros. Sci.* **2009**, *51*, 1172–1180. [CrossRef]

29. *ASTM D1141-98*; Standard Practice for the Preparation of Substitute Ocean Water. ASTM International: West Conshohocken, PA, USA, 1998. Available online: https://www.astm.org/d1141-98r21.html (accessed on 2 February 2024).
30. Alkisswani, L.; Goanță, V.; Munteanu, C.; Samara, F.; Cosau, R.E.; Istrate, B. Considerations on the Failure Mechanisms at Fatigue Loading of 1018 Steel Samples Coated with Wip-C1 by Cold Spray. *Materials* **2024**, *17*, 1868. [CrossRef]
31. Cullity, B.D.; Stock, S.R. *Elements of X-ray Diffraction*; Prentice Hall: Upper Saddle River, NJ, USA, 2001.
32. Ernst, F.; Cao, Y.; Michal, G.; Heuer, A. Carbide precipitation in austenitic stainless steel carburized at low temperature. *Acta Mater.* **2007**, *55*, 1895–1906. [CrossRef]
33. Moridi, A.; Ruan, H.; Zhang, L.; Liu, M. Residual stresses in thin film systems: Effects of lattice mismatch, thermal mismatch and interface dislocations. *Int. J. Solids Struct.* **2013**, *50*, 3562–3569. [CrossRef]
34. Asghari-Rad, P.; Sathiyamoorthi, P.; Bae, J.W.; Moon, J.; Park, J.M.; Zargaran, A.; Kim, H.S. Effect of grain size on the tensile behavior of V10Cr15Mn5Fe35Co10Ni25 high entropy alloy. *Mater. Sci. Eng. A* **2019**, *744*, 610–617. [CrossRef]
35. Ralston, K.; Fabijanic, D.; Birbilis, N. Effect of grain size on corrosion of high purity aluminium. *Electrochim. Acta* **2011**, *56*, 1729–1736. [CrossRef]
36. Liu, W.; Pu, Y.; Liao, H.; Lin, Y.; He, W. Corrosion and wear behavior of PEO coatings on D16T aluminum alloy with different concentrations of graphene. *Coatings* **2020**, *10*, 249. [CrossRef]
37. Matthews, S.; Berger, L.-M. Long-term compositional/microstructural development of Cr3C2-NiCr coatings at 500 °C, 700 °C and 900 °C. *Int. J. Refract. Met. Hard Mater.* **2016**, *59*, 1–18. [CrossRef]
38. Ozkan, D. Structural characteristics and wear, oxidation, hot corrosion behaviors of HVOF sprayed Cr3C2-NiCr hardmetal coatings. *Surf. Coat. Technol.* **2023**, *457*, 129319. [CrossRef]
39. Hernández, H.H.; Reynoso, A.R.; González, J.T.; Morán, C.G.; Hernández, J.M.; Ruiz, A.M.; Hernández, J.M.; Cruz, R.O. Electrochemical impedance spectroscopy (EIS): A review study of basic aspects of the corrosion mechanism applied to steels. In *Electrochemical Impedance Spectroscopy*; Intechopen: London, UK, 2020; pp. 137–144.
40. Lin, C.-C.; Chang, K.-L.; Shih, H.C. Corrosive behavior of chromium carbide-based films formed on steel using a filtered cathodic vacuum arc system. *Appl. Surf. Sci.* **2007**, *253*, 5011–5016. [CrossRef]
41. Prashar, G.; Vasudev, H. A review on the influence of process parameters and heat treatment on the corrosion performance of Ni-based thermal spray coatings. *Surf. Rev. Lett.* **2022**, *29*, 2230001.
42. Liu, S.; Zhu, Y.; Lai, X.; Zheng, X.; Jia, R.; Yuan, X. Influence of different heat treatment temperatures on the microstructure, corrosion, and mechanical properties behavior of Fe-based amorphous/nanocrystalline coatings. *Coatings* **2019**, *9*, 858. [CrossRef]
43. Shrestha, D.; Azarmi, F.; Tangpong, X. Effect of heat treatment on residual stress of cold sprayed nickel-based superalloys. *J. Therm. Spray Technol.* **2022**, *31*, 197–205.
44. Kai, T.; Zhou, X.-L.; Hua, C.; Zhang, J.-S. Oxidation and hot corrosion behaviors of HVAF-sprayed conventional and nanostructured NiCrC coatings. *Trans. Nonferrous Met. Soc. China* **2009**, *19*, 1151–1160.